ANALYSIS OF COMPLEX INTEGRAL PHOTOELECTRON SPECTRA

by

M. P. Panizza B.Sc. (Hons.)

Department of Physics

A thesis submitted for the degree
of Master of Science at the
University of Adelaide

March 1985

awarded 17-5-85

TABLE OF CONTENTS

TABLE OF CONTENTS (continued)

INTRODUCTORY SUMMARY

The major impetus for this thesis is the desire for accurate vibrational branching ratios in the photoionisation of diatomic molecules. These are a sensitive guide to the processes occurring in direct photoionisation and autoionisation. We have the equipment capable of giving low resolution integral photoelectron spectra in the form of steps of various heights. The relative 'heights' are the branching ratios but the shape of the steps change with energy in a fashion peculiar to our own instrumentation. Described within are the various changes and improvements in design and, in one particular area, the optimisation of techniques in the employment of this system presented more fully in Lindemans' Ph.D thesis (1981).

Considerable time was spent, in collaboration with others, on the upgrading of a continuum VUV source. The hoped-for increased intensity would be of great benefit in, generally, low count rate experiments. Though the work was not completed, recent results hold great promise.

With the assurance of increased flexibility and ease of handling, we naturally opted for greater computer control. Paralleling the development of the required interfacing hardware has been the growth of an extensive, though by no means complete, program library. The consequent increased pliancy of the system, hinted at herein, has yet to be fully realised in terms of experimental results.

The bulk of this work falls directly under the given title, the analysis being conducted on a spherical retarding potential photoelectron analyser. This has properties very dissimilar to deflective-type apparatus, most notably, the former having an integral stepped response with electron energy whilst the latter's is differential or peaked. However, like the deflective, there is a specific spectral profile for monoenergetic electrons. The variation of this profile with electron energy has been investigated with the aid of Inert gases and curve fitting. This is shown to be of great benefit in deciphering of partial cross-sections in the more complex molecular spectra, like that of oxygen.

STATEMENT

This thesis contains no material which has been accepted for the award of any other degree or diploma in any university. To the best of the author's knowledge and belief, it contains no material previously published or written by any other person, except where due reference is made in the text.

M. P. Panizza
March, 1985.

ACKNOWLEDGEMENTS

My first handling of the system was done under the anxious eye of Dr W. Lindemans. For his help and the many invaluable discussions on photoionisation, I must express my sincere thanks.

To my supervisors, Dr A.J. Blake and Dr L.W. Torop, I wish to express my gratitude. But for their expert advice and unending patience, this thesis would not be.

As regards the design and construction of the lamp supply, Dr D.G. McCoy and Mr A.L. Jones were always ready and willing to lend an able hand. Messrs B. Fuller and M. Shorthose more than helped in the development of the computer interface. Further unerring technical support was provided by Messrs J. Wright and R. Hurn and many of the workshop and electronic services staff. The fine typing was furnished by Mercia Fuss. To all these people and the many I have forgotten, I am greatly indebted.

CHAPTER I

I. PHOTOIONISATION OF DIATOMIC MOLECULES

I.1 Aspects of Photoabsorption

Of the wide variety of possible interactions between electromagnetic radiation and matter, the one of particular concern to us is photoabsorption by isolated atoms (or, later, molecules); that is, atoms in a gaseous state. In the wavelength range of interest, 60 to 100 nanometres (nm), a part of the extreme ultraviolet, this is by far the dominant interaction.

Electromagnetic radiation comprise photons which can be viewed as packets of energy of a value directly related to the frequency of the radiation, ν.

$$E = h\nu \qquad \text{I.1}$$

$$h = \text{Planck's Constant}$$

Upon photoabsorption of a photon, the atom must undergo an equivalent jump in energy. Figure I.1 exemplifies the simplest of absorption spectra as it varies with frequency. Most noteworthy is a set of discrete lines, at the lower frequencies, which progressively converge on to a threshold, beyond which there is a continuum. The occurrence of discrete lines clearly suggests that only certain energy jumps are allowed here. In the continuum region it is actually possible to obtain a current from the gas by simple application of a small voltage. This is evidence of ion + electron formation, commonly termed

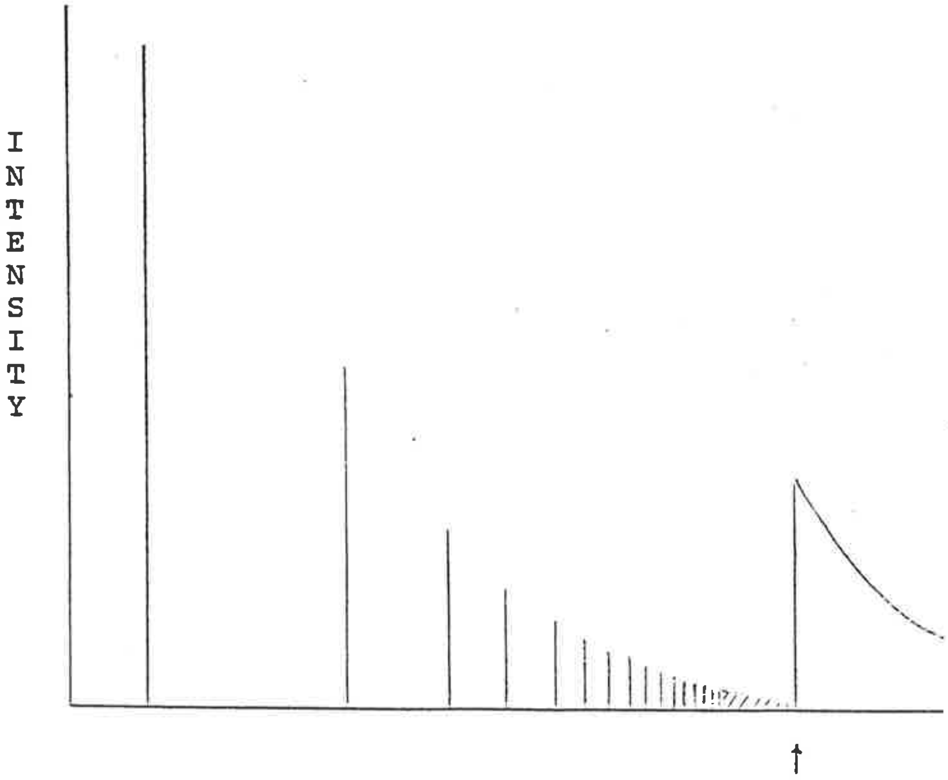

Figure I.1 Schematic of hydrogen absorption spectrum. The shaded section indicates lines too close to resolve. The threshold for ionisation is arrowed.

photoionisation, with the ejected electron becoming a photoelectron. Indeed, upon taking a photoelectron spectrum at a fixed frequency in the continuum domain, a single peak is obtained (again in the simplest case) at a point corresponding to the kinetic energy of the emitted electron. And this energy is very close to the energy difference between photon and threshold, the slight deficit being made up by the K.E. of the ion. Conservation of momentum, before and after the photon-atom interaction, ensures this is the case.

Much of the above is readily inferred from experiment. But for a greater understanding, some theoretical grounding in Quantum Mechanics is necessary.

I.1.1 Aspects of Quantum Mechanics

Before the turn of the century, electromagnetic radiation was largely thought of in terms of waves, as testified by the work of Maxwell. But the concept of a photon developed by Planck and Einstein, suggests a particular nature is more representative at times (e.g., photoelectric effect). Now just as radiation shows this dual character, so it is with matter.

Electron diffraction experiments point to the following wavelength relation:

$$\lambda = h/p \qquad \text{I.2}$$

where p is the momentum. Clearly this wavelike character will only be evident in the atomic realm, where the masses are small enough.

Associated with the wave nature is the Uncertainty Principle, which comes in several forms. For example,

$$\Delta x \cdot \Delta p_x \gtrsim \hbar \qquad \text{I.3a}$$

$$\Delta t \cdot \Delta E \gtrsim \hbar \qquad \text{I.3b}$$

where $\hbar = h/2\pi$, and the Δ's refer to the uncertainties in any measurement of canonically conjugate variables. What it does is basically set a limit to the exactness with which we can define our world. Figure I.2 presents the wave picture, the uncertainty in x defined by the size of an associated wavepacket, and that in p by the spread in the packet's Fourier transform.

To fully describe any wave motion, you need a wave equation. For particles, the appropriate form is found in the Schroedinger Equation.

$$H \Psi (\underline{r},t) = i \hbar \frac{\partial}{\partial t} \Psi (\underline{r},t) \qquad \text{I.4}$$

Ψ , or more strictly $|\Psi^* \Psi|\, dV$, provides a statistical description of the likely whereabouts of the particle of interest. H is the Hamiltonian operator. It's precise form depends on the system being described, but for the simplest case of a single electron moving around a relatively fixed or massive nucleus (essentially the Rutherford picture of the hydrogen atom),

$$H = V(r) - \frac{\hbar^2}{2m} \nabla^2 \qquad \text{I.5}$$

V : potential energy, a function of position (r)

r : distance of electron from nucleus. $r = (x^2+y^2+z^2)^{\frac{1}{2}}$ where (x,y,z) are the co-ordinates of the electron relative to the nucleus.

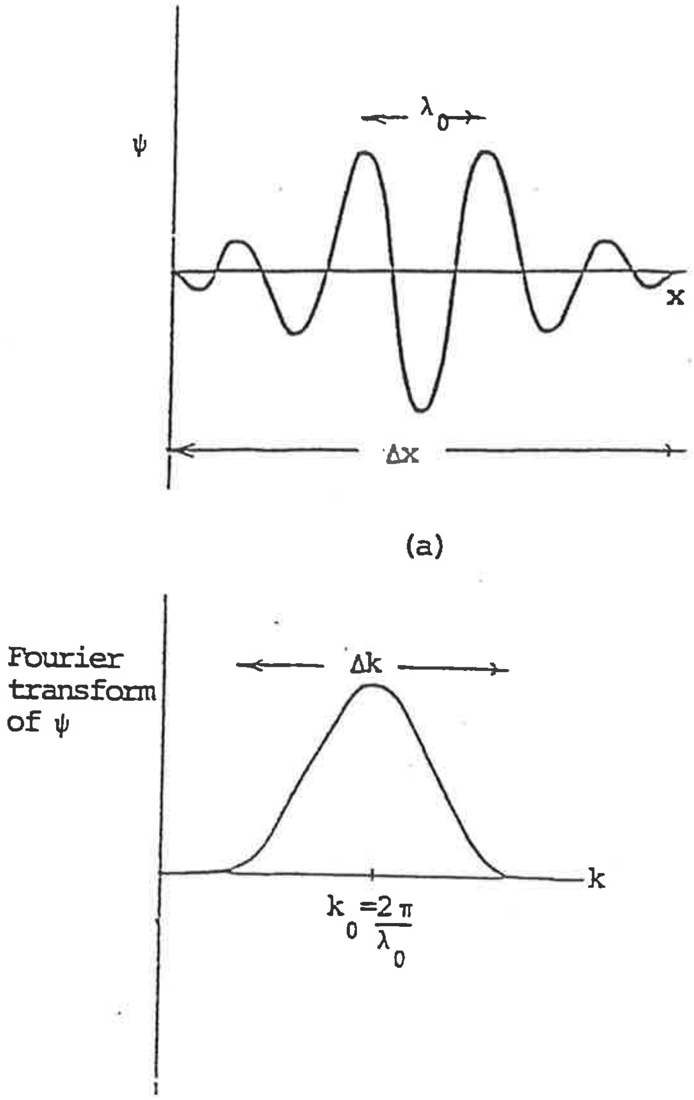

(a)

(b)

Figure I.2 The more localised a particle, the smaller the associated wavepacket. And the larger the spread in wavelengths needed to define it. If Δx tends to infinity, a pure sinusoidal wave would result with only one associated wavelength: $\Delta p=0$.

NB.

$$\Delta k=\frac{2\pi\Delta\lambda}{\lambda^2}$$

$$\Delta p=\frac{h\Delta\lambda}{\lambda^2}$$

$$\Delta p=\frac{h\Delta k}{2\pi}$$

m : electron mass; strictly should use it's reduced mass w.r. to the nucleus.

∇^2 : The Laplacian operator $= \frac{\partial^2}{\partial x^2} + \frac{\partial^2}{\partial y^2} + \frac{\partial^2}{\partial z^2}$

This is basically the sum of potential and kinetic energies respectively. Some justification for this equivalence is given in Schiff (p.20-), through treatment of a free particle. It should be emphasized that there is no strict proof of the S.E., but rather that it relies on it's success in backing up and predicting experimental results.

For an isolated hydrogen atom in a stable state, the S.E. must obey the conservation of energy.

$$H\Psi = E\Psi \qquad \text{I.6}$$

Here E, the total energy of the state, is a constant. As Equation I.4 must still hold, then

$$i\hbar\frac{\partial}{\partial t}\Psi = E\Psi \qquad \text{I.7}$$

implying the separation of Ψ into independent space ($\underline{r}$) and time terms.

$$\psi(\underline{r},t) = \psi(\underline{r})\exp(-iEt/\hbar) \qquad \text{I.8}$$

Equation I.6 can now be solved exactly for ψ, noting that V is in fact the simple centralised Coulomb potential, independent of time. Appropriate boundary conditions ensure the spatial wavefunction mimics real behaviour. For bound states, $\psi \to 0$ faster than $1/r$ as $r \to \infty$, leading to an integrated probability density, $\int \psi^* \psi \, dxdydz$, clearly localised about the nucleus. For ionic states, ψ tends to a plane wave at infinity, corresponding to the untethered electron.

The result is a whole set of possible energy 'eigenvalues' each with their own matching wavefunctions. Below a certain threshold the values are discrete for bound states; above continuous for ionic states. This is as expected from Figure I.1.

The bound wavefunctions, forming a complete orthogonal[1] set, can be well characterised by just three quantum numbers, n, ℓ and m_ℓ. The principal q.n. , n, determines the energy, and runs through the Natural numbers to infinity at threshold. ℓ has values of 0,1,2, ..., n-1 for a given n and defines the allowed orbital angular momenta, $L = \sqrt{\ell(\ell+1)}\,.\,\hbar$. Finally m_ℓ ranges from $-\ell$, $-|\ell-1|$, ... , -1,0,1 , ..., ℓ and corresponds to the component of L in a particular direction, for example, an external magnetic field, giving $L_z = m_\ell \hbar$. Loosely the wavefunctions can be thought of as localised to certain orbitals or regions of increasing radii with n and decreasing 'spherical symmetry' with L. On the face of it,[2] for a given n, the energy levels are equivalent or 'energy degenerate, independent of ℓ and m_ℓ. This degeneracy is readily removed by the application of an external magnetic field which interacts with the angular momentum components.

---

[1] $\int \Psi^*(n_1, \ell_1, m_{\ell 1})\Psi(n_2, \ell_2, m_{\ell 2})\, dV = 0$ if any of the 3 q.n.'s differ; i.e. for different states.

[2] A closer look at the hydrogen spectrum reveals a fine structure in the supposedly degenerate levels. The explanation lies in a fourth q.n., $m_s = \pm \frac{1}{2}$, relating to an electron spin that weakly interacts with the orbital angular momentum - a spin-orbit effect. This becomes more important for multielectron atoms.

Besides energy and angular momentum, ψ contains all the information you can possibly expect to extract without disobeying the Uncertainty Principle. For instance,

$$\bar{r} = \int \Psi^* \, r \, \Psi \, dV \qquad \text{I.9}$$

gives the average radius, readily comparable to the Bohr radius for the lowest energy, or ground, state. Note that: dV is a volume element best expressed in spherical polar co-ordinates; r is the distance from the nucleus, the origin of the co-ordinate system; and that the integration must take place over all space. In fact the average or expectation value of any real observable quantity is easily found in a similar fashion, as long as the correct operator is known. That for energy has been seen in the Hamiltonian. The appropriate one for momentum can thus be inferred, giving

$$\bar{p} = \int \psi^* \, . \, -i\hbar \, \nabla\psi \, dV \qquad \text{I.10}$$

For multielectron atoms, H becomes

$$H = V(r) - \frac{\hbar^2}{2m} \sum_j \nabla_j^2 \qquad \text{I.11}$$

where the summation is for each electron. V is no longer the simple centralised Coulomb potential as individual electrons now provide a repulsive force. The resulting S.E. has no analytic solution, in much the same way as the classical three-body problem of astrophysics. The alternative is to start with a few approximations. Initially it is assumed that each electron can be treated independently, moving in some average potential of the nucleus and the other electrons. This allows the total spatial wavefunction to be separated into a product of individual electron wavefunctions.

$$\psi = U_1 U_2 U_3 \ldots U_n \qquad \text{I.12}$$

It is further assumed that the potential is spherically symmetric, strongest, naturally, near the nucleus but falling off rapidly as you move out, due to the 'shielding' of the nuclear charge by the other repulsive electrons. Eventually, at large r, the potential is hydrogen-like, decreasing as 1/r. Also for multielectron systems, a new postulate must be added to the S.E. if results are going to be representative of real systems. That postulate is the Pauli Exclusion Principle. It simply says that no two electrons can be in the same state. This stops all the electrons simply falling into the lowest possible state.

The S.E. can now be solved for the individual electron wavefunctions. From the ensuing probability densities, the closely related charge densities can be found. This provides a new potential picture, readily compared with the original. If different, the new potential replaces the old and the wavefunctions are recalculated. The process is repeated again and again, until a consistent potential is found.

The method described is basically that of Hartree (1928). The picture that unfolds is of an infinite set of bound wavefunctions similar to the hydrogen wavefunctions (same n, ℓ, m_ℓ), with their corresponding suborbitals progressively filled in order of energy by two electrons of opposite spin. Importantly, electrons of the same n but different ℓ no longer give rise to degenerate levels. The greater core penetration* of the lower ℓ electrons binds them more tightly. This relatively simple method provides a good understanding of the Periodic Table with only the outermost electrons significantly involved in bonding.

A refinement over the above treatment, by Fock (1930), allows for the indistinguishability of any two electrons. Thus labels on individual electron wavefunctions can be freely exchanged. The method makes use of a stronger form of the Pauli Exclusion Principle, that the total wavefunction must be antisymmetric. The energy eigenvalues so obtained provide a very good first approximation to the true energy levels.

The treatment for continuum states is in two parts. First the wavefunction for the isolated ion is found in equivalent fashion to the above. Now the ejected electron can be treated as being scattered by the average charge distribution of the ion, with due allowance for exchange (Manson, 1978). Clearly the asymptotic behaviour of the unbound waveform is uniquely determined by the given total energy and the ion's energy levels.

---

* If all the orbitals up to a certain n are filled, they form a spherically symmetric cloud or core about the nucleus, thus shielding the outer electrons from it's strongly binding, positive charge. However, all 'outer' electrons must spend some time near the nucleus within this core.

Figure I.3 is a schematic of the resulting complex energy levels typical of multielectron atoms. Several series are apparent, converging on differing ionisation potentials. The higher I.P.'s are excited states of the ion. They may be thought of as arising from the excitation of an inner electron, with the reduced shielding of the core leading to stronger binding and a higher I.P. An accompanying photoelectron spectrum clearly maps out the populations of the various ionic levels.

There are a number of important effects that the above fails to account for, effects that show up in the finer detail of spectra, for example, electron correlations. Let us say that two electrons tend to keep on opposite sides of an orbit. They obviously do not move in the average potential of one another and strictly cannot be treated as independent. And of particular importance, there are spin-orbit effects. Rigorously speaking, individual orbital and spin angular momenta are not quantised, only their vectorial sum involving all the electrons. But even here matters can be greatly simplified with only the outermost electrons effectively taking part in the sum, the spherically symmetric core contributing 0 (Banwell, 1972).

Both the above effects can be accommodated into the Hartree-Fock picture, and result in a small shift and splitting of the energy eigenvalues, nicely matching experimental data. However, this does not guarantee that the correct wavefunctions have been found. A case in point is the spin-orbit effect apparent in Rare gas spectra

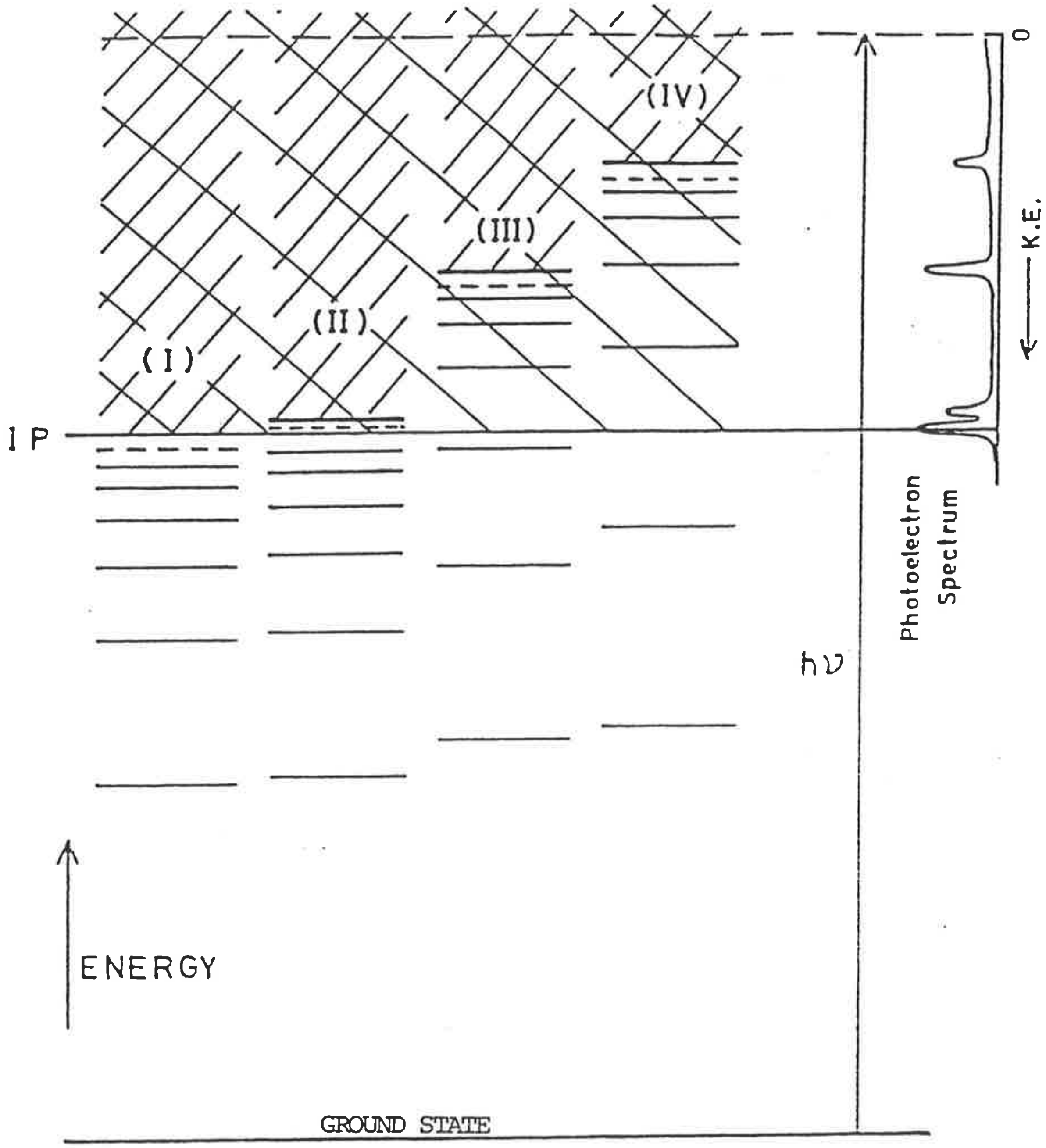

Figure I.3 Atomic energy level diagram showing four series of levels. Each converges to a different continuum threshold. The adjacent photoelectron spectrum shows how the energies of these levels can be directly mapped.

(Chapter IV). The expected splitting is easily accounted for. But a better test for the correct wavefunction is the branching ratio in the population of the two states. More accurate estimates than the Hartree-Fock's are often obtained through the use of semi-empirical parameters. (Lu (1971) using quantum defect theory.) To understand the importance of branching ratios (relative transition rates), consider the following.

Absorption of radiation involves changes with time, and as such must be treated by time dependent perturbation theory using Equation I.4. For weak radiation the treatment is semi-classical, with the polarising electric field of the electromagnetic wave acting as a small perturbation to H, leading to a mixing of states. It is a relatively simple derivation, duplicated in many a quantum mechanical text (Marr, p.40), to show that the transition rate between two states is given by

$$P(f \leftarrow i) = \frac{2\pi^2}{3h^2\varepsilon_0}\rho(\nu)\left|\int \psi_f^* e\underline{r} \psi_i dV\right|^2 \qquad \text{I.13}$$

$P(f \leftarrow i)$: probability of transition from initial to final state.

ε_0 : permittivity of free space.

$\rho(\nu)$: radiation density for given frequency.

$e\underline{r}$: electric dipole of active electron relative to nucleus.

The frequency must correspond to the energy difference between the two states (Equation I.1). Without going into the details of the two states, symmetry requirements and the conservation of angular momentum can often tell us a lot about the allowed transitions. The selection rules for multi-electron atoms are indicative of this.

$$\Delta S = 0 \qquad \text{I.14a}$$

$$\Delta L = \pm 1 \qquad \text{I.14b}$$

$$\Delta J = 0, \pm 1 \qquad \text{I.14c}$$

S : spin angular momentum
L : orbital angular momentum
J : total angular momentum

For branching ratios, when there are two possible final states, Equation I.13 can be simplified considerably. Generally there is no need to know $\rho(\nu)$, and thus no difficult calibration of the experimental system. And if the two final states are similar then relevant parts of ψ_f may be separated out and ignored. This is a technique of particular importance to molecular studies.

I.2 Diatomic Molecules

Much of the previous sections is readily applicable to diatomic molecules. However, the treatment is complicated by the possibility of the relative motion of the two nuclei involved. These are in the form of vibration and rotation. Also upon excitation of the molecule, several processes may compete in the absorption of the energy. Besides transitions to some higher electronic state, for photons of sufficient energy, dissociation can occur.

In spite of these complications or, in a sense, because of them, molecular spectroscopy is in some ways simpler than atomic. Quite simple measurements can supply a lot of information about diatomic systems. This arises in a large part from the viability of the Born-Oppenheimer Approximation, which allows the separation of the molecular wavefunction into electronic and nuclear components.

$$\psi = \psi_e \quad \psi_n \qquad \text{I.15}$$

In physical terms, this separation exemplifies the marked distinction in the natural frequencies of the two motions, an electron completing about a hundred orbits in the time it takes for a single vibration. It is a bit misleading to speak of the separation of these wavefunctions. A little thought must show that ψ_e is a function of the nuclear spacing. But Born and Oppenheimer (1927) showed their approximation holds true, as long as the variation in ψ_e with internuclear separation is slow enough, which is generally the case. Thus the molecule's total energy is related by

$$E = E_e + E_n \qquad \text{I.16}$$

The nuclear wavefunction itself can be further divided into vibrational and rotational components. Strictly they are not independent, the proper treatment being that of the vibrating rotator (Marr, p.119). But in any event, the vibrational effect dominates. In fact the rotational levels contribute no observable effects to our spectra, and can be largely ignored.

Figure I.4 pictures some of the more important allowed energy states of oxygen. The various electronic states determine the total potential energy of the nuclei for a given internuclear separation, leading to the curves that dominate the diagram. For stable molecular configurations a curve must have a minimum. The shape of such curves is generally quite well described by the Morse potential (Morse, 1929). Stelle _et_ _al_. (1962) compares _his_ treatment with a variety of more recent mathematical models. The allowed vibrational wavefunctions can now be found by the quantised treatment of a linear oscillator in a given potential well (Figure I.5). Figure I.4 shows that bound ionic states are also possible.

I.2.1 Franck-Condon Factors

At room temperature the Boltzmann distribution ensures that essentially all oxygen molecules are in the ground state - in vibrational level v_0. Thus in any transition of interest, this will be the initial state.

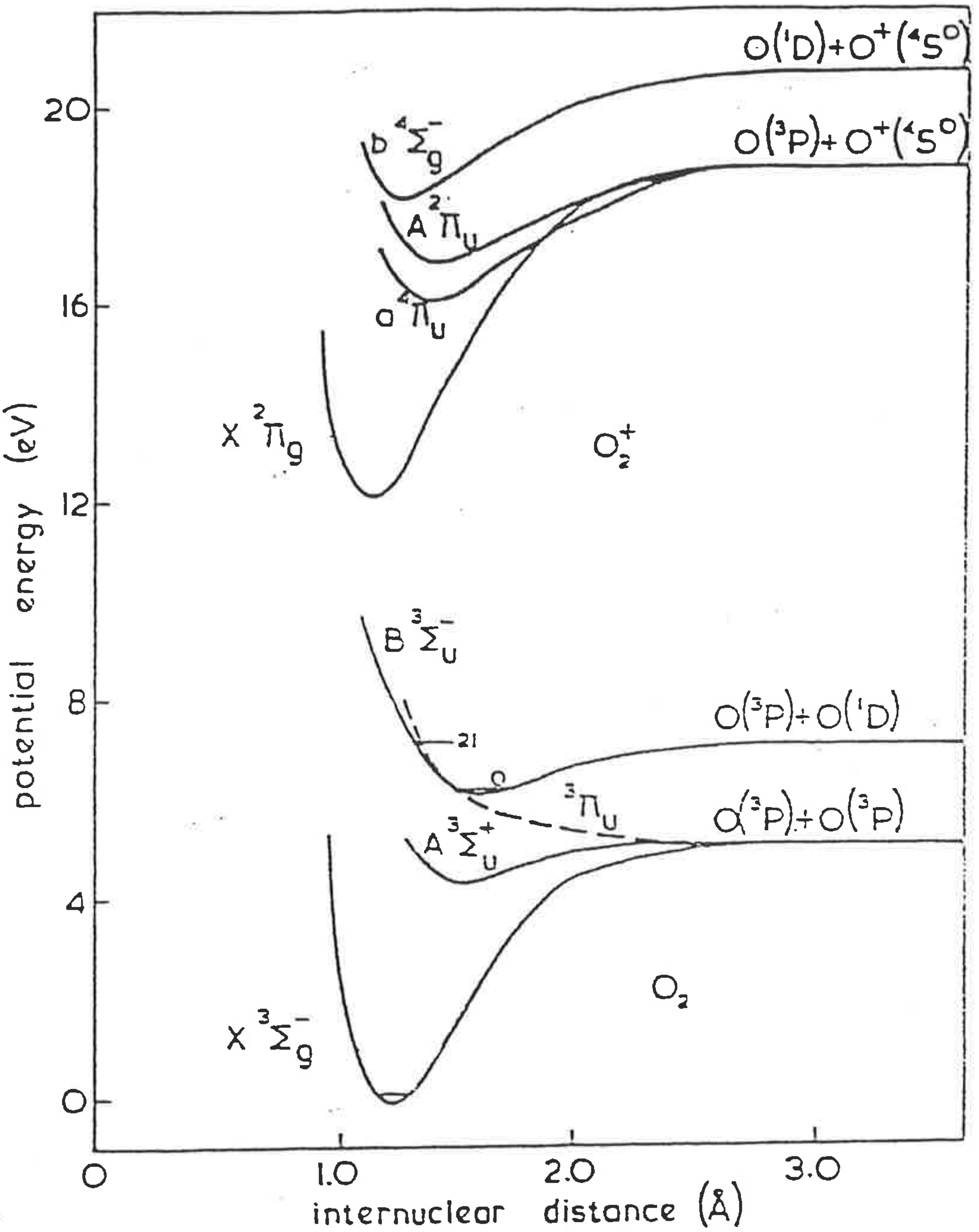

Figure I.4 The major electronic states of molecular oxygen. Note that the $^3\Pi_u$ state is an unbound or dissociating state. Diagram from Marr (1967).

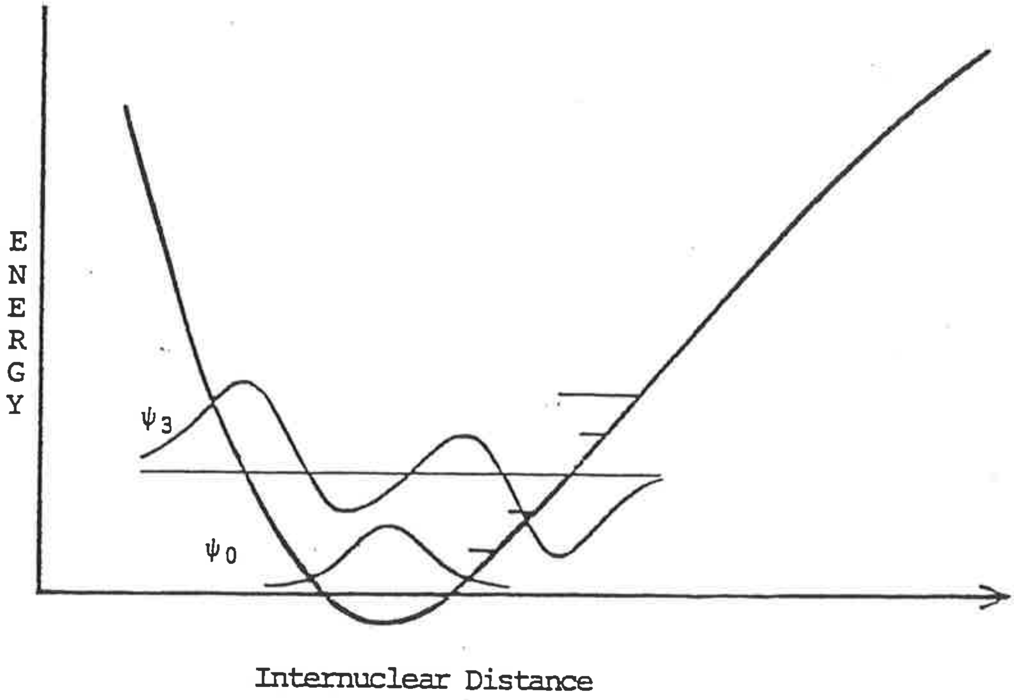

Figure I.5 The resulting vibrational wavefunctions for the 0th and 3rd vibrational levels. The potential curve is defined by the electronic state. Note that these wavefunctions are real.

And the final states of particular interest are the various vibrational levels for a given ionic state.

Equation I.13 is easily extended to the molecular case by noting there are now three charge centres involved in the dipole formation (Herzberg, p.199). Considerations of orthogonality and the independence of the nuclear dipole from the electron's co-ordinates, quickly leads to

$$P(2 \leftarrow 1) \propto \left| \int \psi_e^{2*} \psi_v^2 \; e \, \underline{r} \; \psi_e^1 \, \psi_v^1 \, dV \right|^2 \qquad \text{I.17}$$

Now assuming that the electronic transition moment is independent of the internuclear separation, this gives

$$P(2 \leftarrow 1) \propto \left| \int \psi_e^2 {}^* \; e \, \underline{r} \; \psi_e^1 \, dV_e \quad \int \psi_v^2 \, \psi_v^1 \, dr_v \right|^2 \qquad \text{I.18}$$

$$= \left| D_e \int \psi_v^2 \, \psi_v^1 \, dr_v \right|^2 \qquad \text{I.18a}$$

dV_e : volume elements of the space for electronic co-ordinates.

dr_v : vibrational wavefunctions depend only on internuclear distance.

This simply states that the relative intensities of transitions to various vibrational levels, within the one ionic state, depend solely on the respective vibrational overlap integrals - on the Franck-Condon Factors.

A physical description is provided by the Sudden Approximation. Electronic transitions can be said to take place so fast that the nuclei do not move in the transit. Thus the most populated vibrational level is that directly 'above' the ground state. Figure I.6 describes the state of affairs better than words.

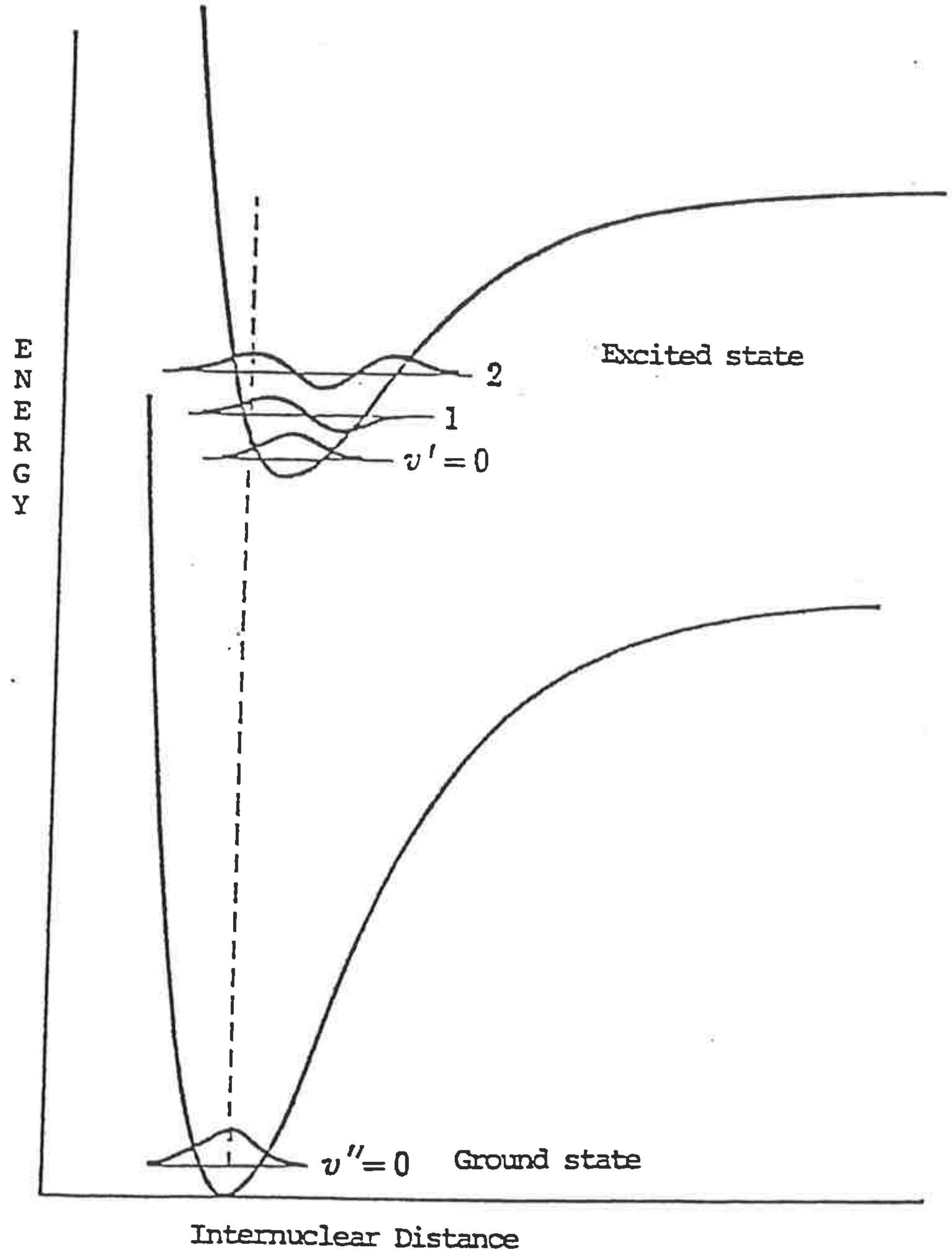

Figure I.6 Schematic of the Franck-Condon Principle. For transitions from the ground state to the upper excited state, the greatest overlap occurs for the 2nd vibrational level, as is indicated by the broken vertical line. Reproduced from Herzberg P.199 (1950).

What this means experimentally is that a set of relative vibrational intensities can be used to describe the ionic state they came from, as they provide information on each of the ψ_v^2 . However, glancing back at Equation I.18, it must be pointed out that it's form rests solely on the assumption of a constancy of D_e with respect to internuclear spacing. More realistically, it is a slow function of this separation. Thus, given knowledge of the ionic state being populated, relative intensity values at variance with the Franck-Condon factors, act as a measure of this variation in D_e . Please note that the above applies strictly to direct photoionisation to the continuum.

I.3 Autoionisation

Glancing briefly back at Figure I.3 it should be readily apparent that there are discrete bound states or resonances, converging on to the higher ionisation potentials, with energies equivalent to continuum states. These levels can be excited after the normal fashion for discrete levels. But instead of them radiatively decaying back to the lower levels in the order of 10^{-8}sec., the possibility often exists for a radiationless jump over to the continuum in the order of 10^{-13}sec. This process, known as autoionisation, provides an alternative and competing pathway for photoionisation to the direct path described previously. Experimental evidence for autoionisation is found in the broad enhanced ionisation resonances seen in many atomic and molecular spectra (Figure I.7). The width of such resonances (if they are sufficiently isolated) can be loosely related to the time taken for the radiationless jump, by the Uncertainty Principle (Equation I.3b).

One of the earliest and simplest theoretical treatments is that provided by Fano (1961). Of all the major theories, his provides the best physical understanding of what is going on. According to him, for a single line interacting with a single continuum, the true state of a system at energies near the expected discrete line's energy, is given by a mixture of the continuum and discrete states. The simple though approximate Hartree-Fock wavefunctions can be put to good use here in deriving

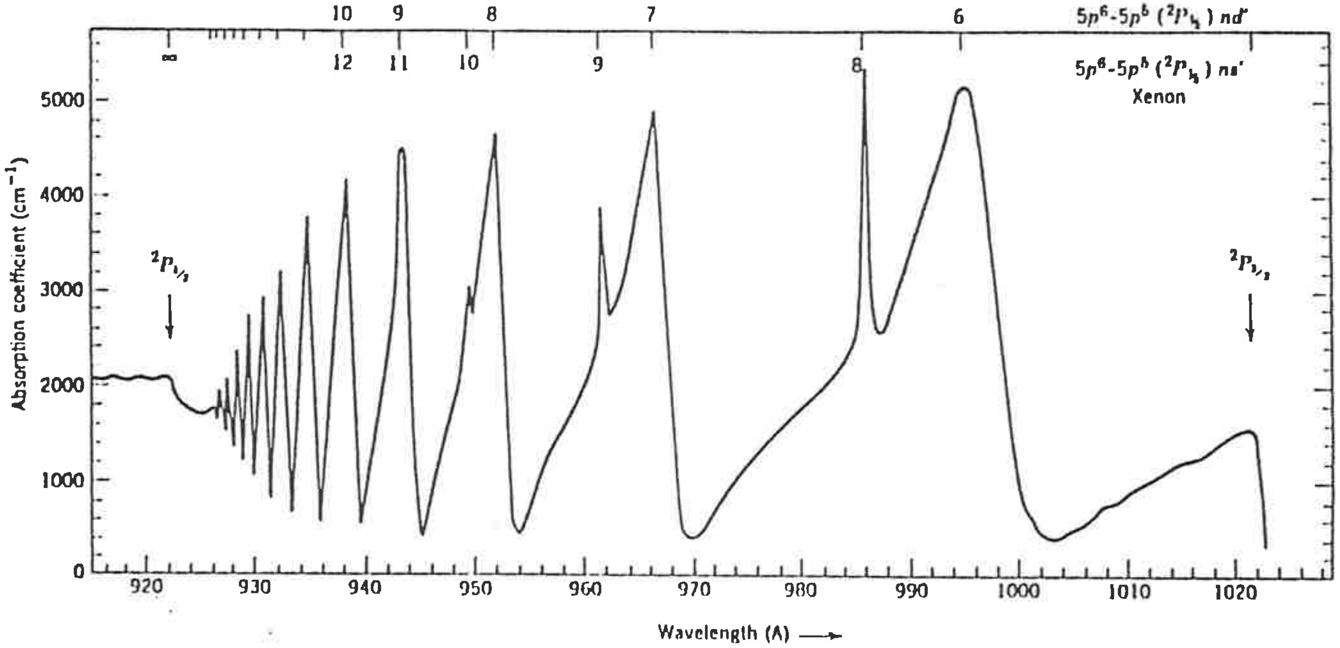

Figure I.7 An infinite series of Beutler autoionising resonances converging onto the upper spin-orbit component of xenon. Actually there are two series evident here. Note the asymmetry of the profiles.
From Huffman *et al* (1963).

the correct mixture* (Torop, 1975). Now when considering transitions to this complex state, the variation in cross-section with wavelength can be related to interference effects between the continuum and discrete components. The resulting characteristic broad asymmetric profile is named in Fano's honour. It is well described by just two parameters. One from the width, relates to the strength of the coupling between discrete state and continuum or, inversely, to the average period for transition. The other from the intensity relates to the proportions of autoionisation and direct photoionisation.

A single resonance and a single continuum is certainly the exception rather than the rule in photoionisation studies. For the general case of several overlapping resonances and several continua, Mies (1968) must be consulted. Extra parameters are needed to allow for continua that do and do not interact with the resonances and to allow for interference effects between neighbouring resonances. Parameter fitting can become exceedingly difficult if resonances are too crowded.

For the molecular case autoionising resonances generally dominate the total photoionisation spectra. A tell tale sign in photoelectron spectra is vibrational branching ratios showing marked deviation from the expected Franck-Condon Factors, notably in the higher

---

* Although H-F's are not the correct wavefunctions, they do form a complete orthogonal set, and as such the true states are given by linear combinations of these wavefunctions.

vibrational levels (Figure I.8). However, these factors can still be applied at the peak of an isolated resonance by considering the intermediate transitions from ground to discrete state and from there to continua (Smith, 1970).

$$I_f \propto F_{gf} + F_{ga} \cdot F_{af} \cdot q^2 \qquad \text{I.19}$$

F_{gf} : F-C factor for transitions from ground to final vib. level.

F_{ga} : F-C factor between ground and autoionising state.

F_{af} : F-C factor between autoionising state and final vib. state.

q : Describes proportioning between autoionisation and direct photoionisation and is independent of the vibrational level for a given electronic state.

Through the correct use of this formula it is possible to extract a lot of information about the autoionising state. However, a closer look at the theory, as provided by Lindemans Ch. VIII (1981), shows that much more information is found in the variation of these branching ratios with wavelength right across a resonance or series of resonances. In such instances there can be marked contrast between different vibrational levels.

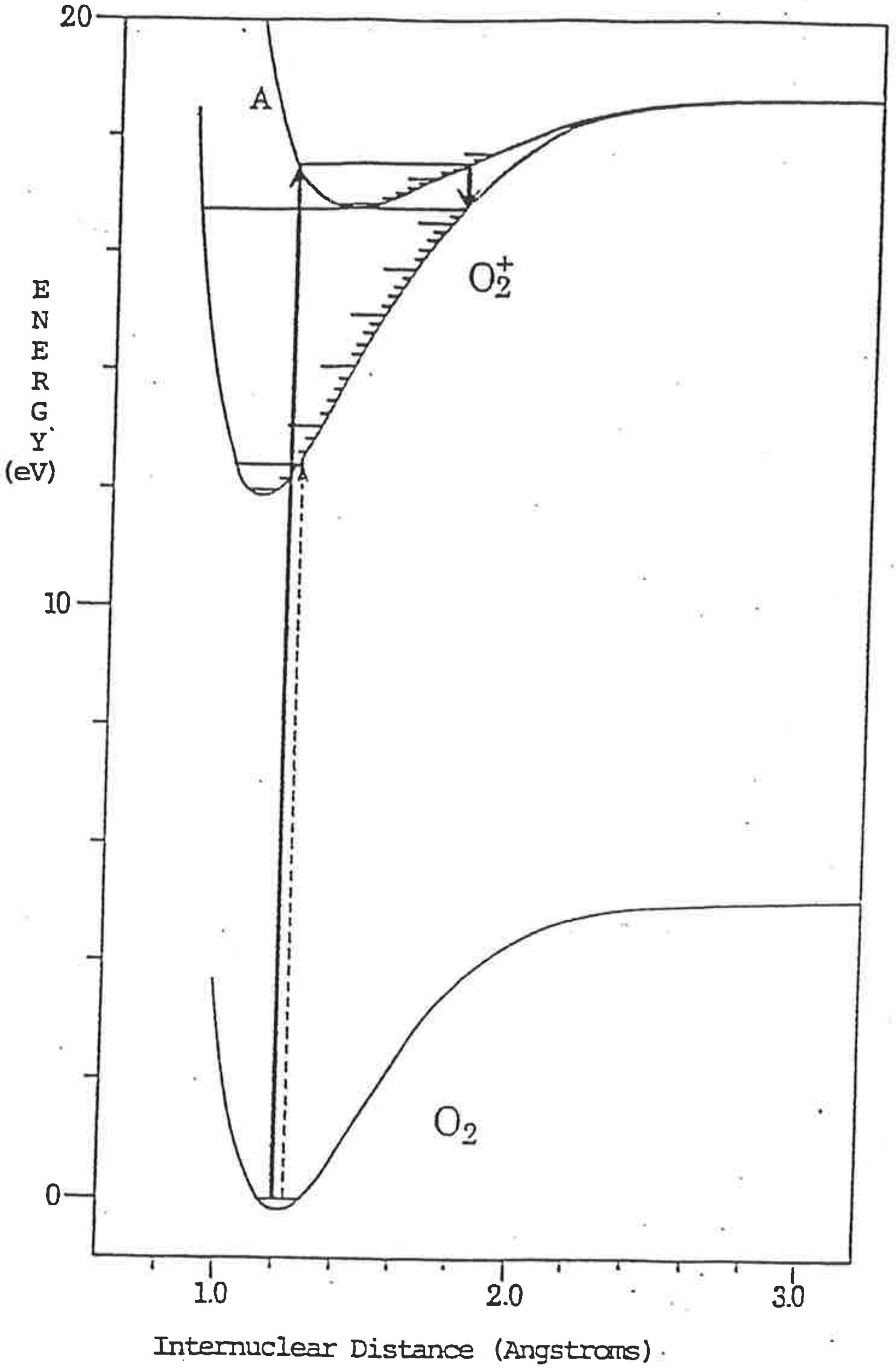

Figure I.8 Production of high vibrational states in the oxygen ion via the autoionising state A. Peaks in the photoelectron spectrum can be expected at v_2 and v_{27}. The dashed line indicates direct photoionisation. After Smith (1970).

CHAPTER II

II. THE EXPERIMENTAL SYSTEM

A critical part of this work is the mastering of the complex equipment needed to obtain experimental results. In the form that I found it, the instrument had many strong points and but a few limitations, in terms of taking branching ratios in the region from 60 to 100 nanometres.

A brief overview is presented of the special features that make the system so useful, with extra detailing of those areas requiring improvement, and the measures that have been taken.

II.1 Design of the Instrumentation

For the two major atmospheric gases, molecular oxygen and nitrogen, the region from 100 to 60nm contains a wealth of autoionising structure. Total absorption and photoionisation cross-sections can now be taken to show this (Dehmer and Chupka, 1975). But, as Section I.2.1 indicated, the bulk of the information is hidden away in the continuum partial cross-sections, particularly those pertaining to vibrational levels. These require energy analysis of photoelectrons, which compare unfavourably in count rate with the total cross-sections of ion yields (above reference). Thus low count rates are involved, which must be overcome.

Figure II.1 lays out the original basic instrumentation, and should be referred to repeatedly throughout this section. Beginning briefly with the UV lamp, a condensed spark Helium discharge provides a continuum source over the requisite range (actually defines the range), but like any continuum source, low light levels are the rule. Attempts to improve this situation are presented in Section II.2.2a.

Not shown in the diagram is the extensive differential pumping needed to maintain the enormous pressure gradient between lamp and vacuum monochromator, as there are no known windows in this wavelength region.

Dispersion of the light is provided by a McPherson one-metre near normal incidence vacuum monochromator. With

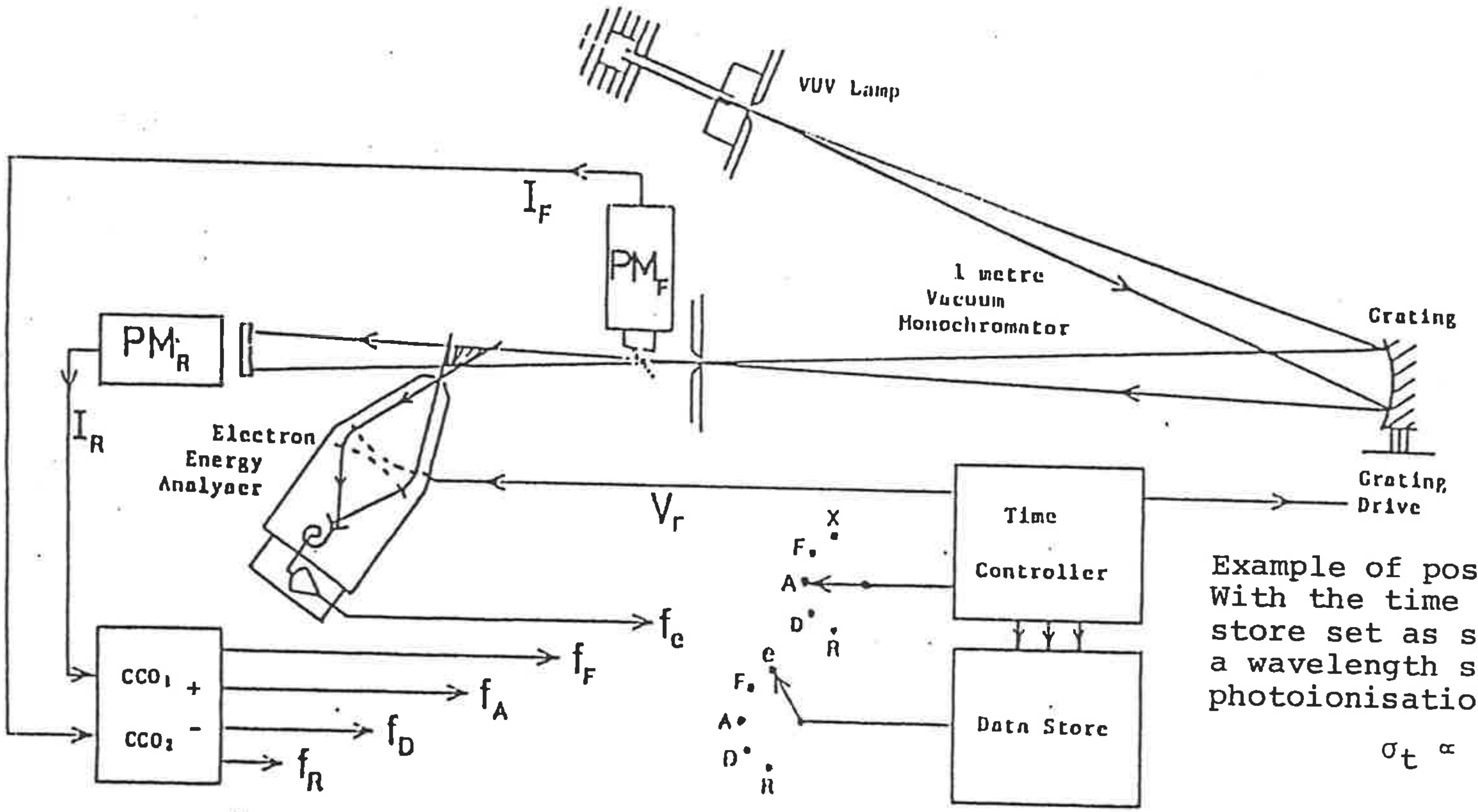

Example of possible measurement:
With the time controller and data store set as shown and $V_r=0$, a wavelength scan gives the total photoionisation cross-section.

$$\sigma_t \propto f_e/f_A$$

Figure II.1 Schematic of the experimental system:
V_r is the retarding potential applied to the analyser, f_e is the frequency of photoelectrons detected, f_F and f_R are frequencies proportional to the front and rear light signals, f_A and f_D to their average and difference. Any of these signals may be applied to the time controller or the data store.

a 1200 lines/mm concave grating and a 0.1mm entrance slit, this gives a 0.83nm/mm first order dispersion at the exit. This entire set up has the highly desirable property of supplying a nearly undeviating exit beam, the need for which is not just practical (see below for angular distributions of photoelectrons).

Then there is the all important ionisation region, to where the gas under examination is introduced. Front and rear photomultipliers allow light levels to be accurately monitored in the central interaction region (shaded), provided absorption does not exceed 30%. Otherwise a non-linear response occurs (Lindemans, 1981, p.141). In fact four signals are generated from the two tubes, increasing the system's flexibility.

The electron energy analyser has a wide acceptance cone, allowing for the low count rates mentioned earlier. An important property of photoelectrons is that they are not produced isotropically. Indeed, under unpolarised light, there is a continuous range of possible distributions. (Yang (1948) for plane polarised light; for unpolarised light rotate distribution about direction of beam.) This could easily lead to distorted branching ratios, but for the presence of a 'magic angle' (Figure II.2), namely 54° 44', which yields reliable relative intensities unaffected by the exact distributions of the individual partial cross-sections, or how they vary with wavelength. Thus the analyser is placed at 55° 50' to the light beam in the horizontal plane, a slightly modified

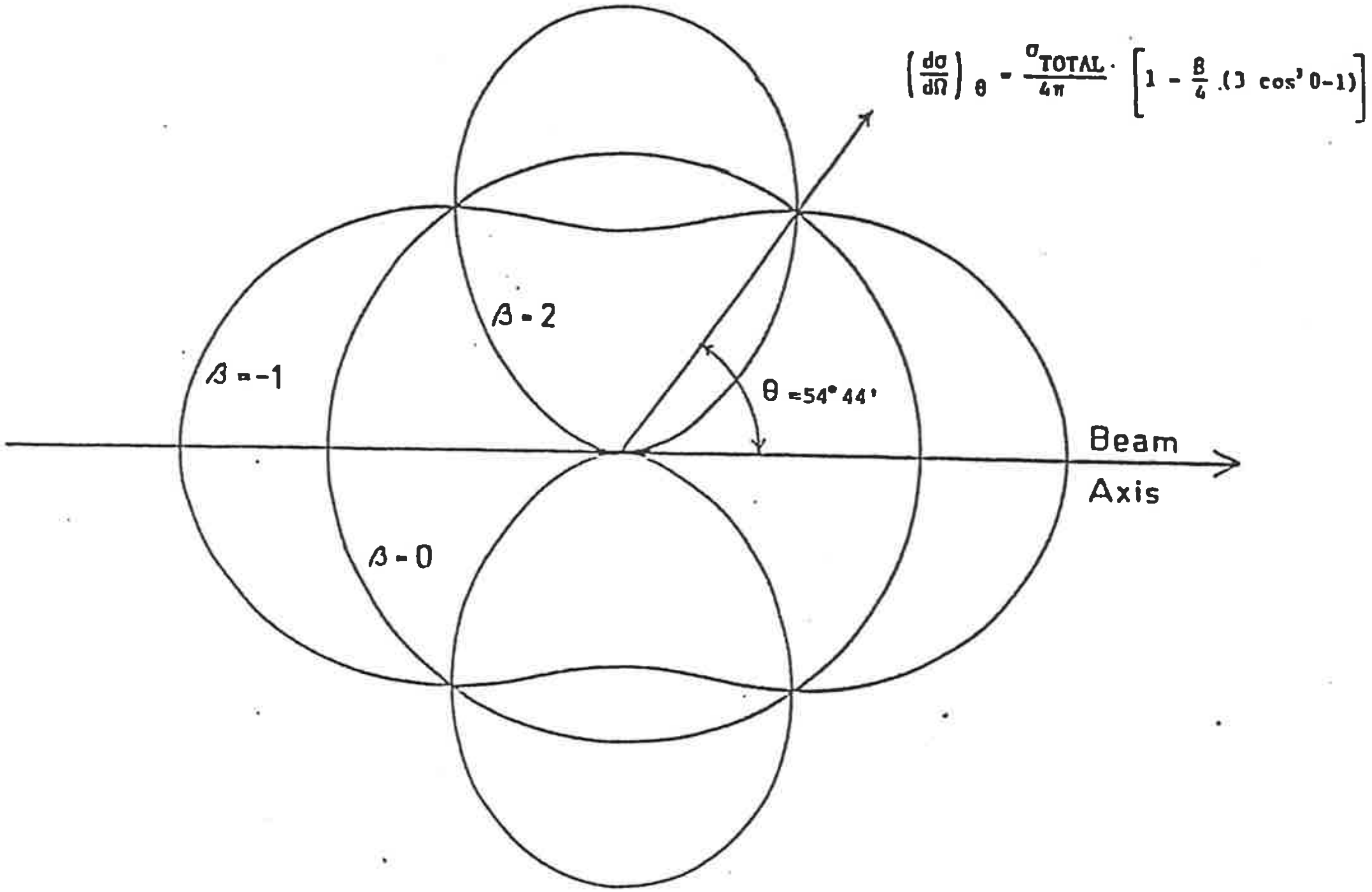

Figure II.2 Polar diagram of Differential Cross-section of Photoionisation with unpolarised light and three values of β. Note that the figures are curves of rotation about the beam axis.

angle allowing for an extended, as opposed to point, source and for the large acceptance cone of the analyser (Lindemans, 1981, p.151). As the above applies to unpolarised light, there is also the problem of our vertically ruled grating giving rise to a partially polarised beam. The degree of this polarisation varies with wavelength (Samson, 1978), again playing havoc with electron distributions. This is guarded against by placing the analyser 45^{o} from the horizontal. Other properties of this remarkable piece of apparatus shall be detailed in the next chapter.

And, finally, we shall discuss data collection. There are five signals available for counting, giving an impressive array of possible experimental set-ups. Notably, measurements like the yield, f_e / f_D , are important in the calibration of the system (Lindemans, 1981, p.160). However, only two signals are available for processing at any one instance, an unnecessary and time-consuming limitation. There are two control lines allowing wavelength and retarding potential (related to electron energy - see Section III.1) to be advanced concurrently in a linear fashion, as needed for continuous partial cross-sections. Strictly, the retarding potential should follow an inverse law in such instances.

$$E = hc/\lambda - \text{I.P. (constant)} \qquad \text{II.1}$$

The answer to these problems is in Section II.3.

II.2.1 UV Line Sources

These sources correspond to atomic transitions and are characterised by their relative brightness and extreme monochromacity. They are readily excited by a DC discharge (Figure II.3a) through the appropriate atomic gas, provided molecular impurity levels are low. An important point to remember is that a negative voltage be used, to avoid damage of the entrance slit by ion bombardment. Other problems are pressure broadening and self-absorption but these are easily overcome by reducing the pressure until no change in line shape is evident.

All experiments presented in this book, with which I have been directly involved, were performed with line sources. In the past they have played a very important part in partial photoionisation studies. Increasingly, though, continuum sources are being deployed, for reasons already mentioned (Section I.3). This leads naturally into the next section.

II.2.2 A Continuum Source

The Hopfield continuum of helium has a useful wavelength range of 60 to 100nm. This ensures few problems in the way of 2nd order effects unlike the extensive Synchrotron sources (West *et al.*, 1974). It's excitation involves the formation and rapid decay of helium molecules, via several stages of interaction (Tanaka, 1942).

High current densities are needed, making a pulsed supply necessary.

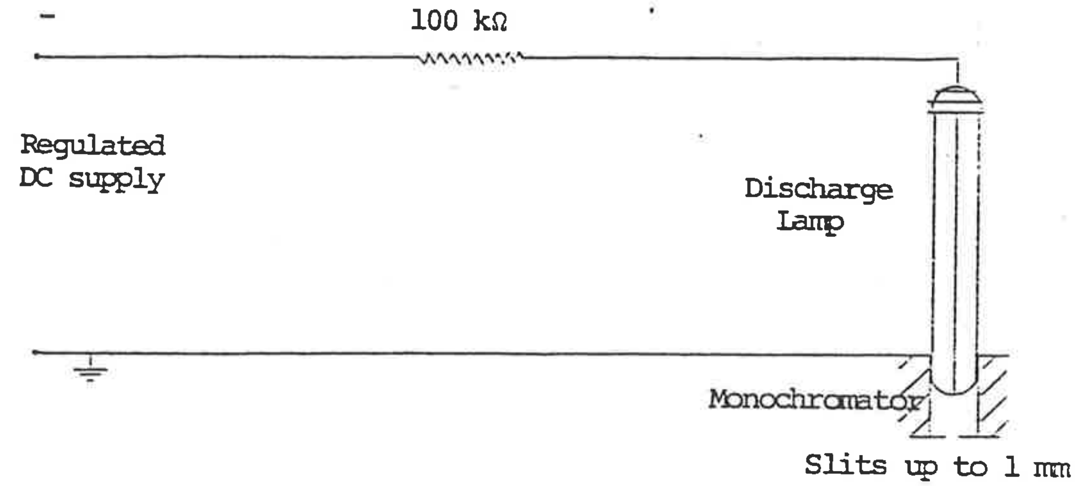

Figure II.3a Schematic of DC lamp. Typical currents of 15 mA used but limit set by channeltron linearity.

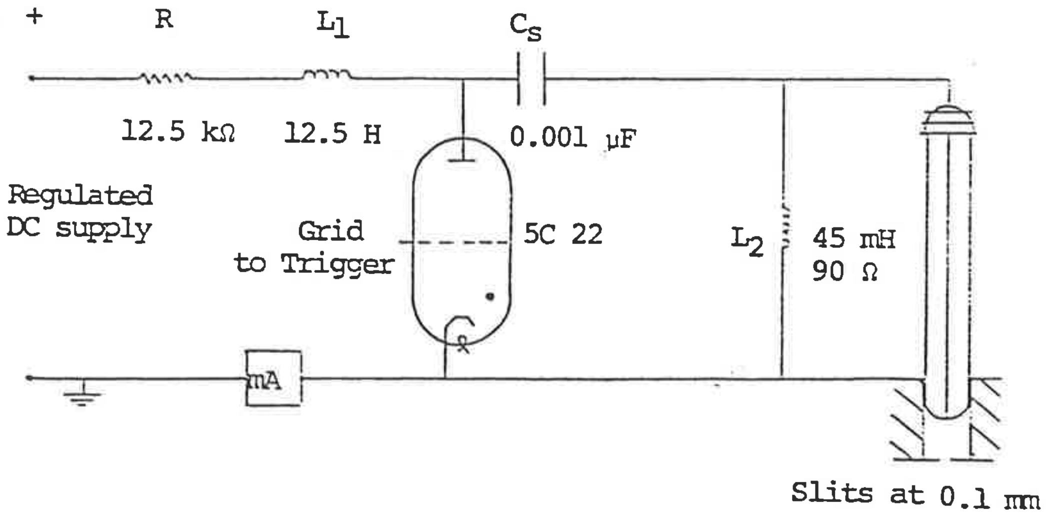

Figure II.3b Schematic of old pulsed supply. Optimal lamp frequency of 5 kHz.

Figure II.3b lays out the original circuit. Initially the underdamped LRC circuitry charges up the spark capacitance with a ringing frequency of about 2.5kHz. But as soon as peak voltage is reached, the thyratron is 'fired', by applying a positive pulse to it's grid, grounding one side of C_s and quickly switching it's stored charge through the lamp. Thus the pulsing frequency is 5kHz. Note that during firing, L_2 acts as a very high impedance. Once the capacitor is discharged, the thyratron should quickly go open circuit.

II.2.2a A Brighter Continuum Source

There are four major options available to us in developing a brighter lamp. One is to increase the capillary length, since there can be no self-absorption of the radiation being produced (see reference above of the complex excitation mechanism). A narrower capillary bore is also of benefit with it's increased current density. All this was, in fact, done by Martin (1981) with positive results. Further modifications in this area, however, could run into problems of construction and in initiation of the discharge.

Another option is to increase the operating pressure from 50T to some more appropriate higher value dependent on the electrode configuration (Huffman et al., 1965). Closely related to this is the width of the entrance slit used. The narrower the slit, the higher the pressures that can be sustained; the wider the slit, the greater the light flux for a given pressure. But for the current differential pumping system, the balance between slit width and pressure would appear to be about optimal.

The other two methods involve changes in the electronic circuitry powering the lamp. Either the pulsing frequency or the voltage must be increased. The former results in a linear increase whilst the latter gives an approximately quadratic increase. The greater gain with voltage must be weighed against a shortened thyratron life, an enhanced noise or ground current, and, in the extreme, non-linear counting.

Any straightforward attempt to improve the original circuit's (Figure II.3b) light output immediately encounters problems. Every thyratron has an associated anode heating factor, the product of peak anode voltage, peak instantaneous current, and the pulsing frequency. As this is approached by, say, increasing the frequency, the resulting raised temperatures lead to a resistive loading and increased recovery time (Thyratron Preamble, 1972). Eventually a point is reached where the thyratron fails to fire every cycle, dropping the light output.

Now it would seem but a simple matter to deploy a thyratron with a greater anode heating factor. But upon doing this, with the CX1159, any chance of success is lost by the occurrence of 'latching'. When a tube fires, the anode voltage drops rapidly to near zero and may even go negative. The internal plasma now has a chance to decay, turning off the switch. However, if the rebuild-up of voltage is too rapid, as would tend to happen in any high frequency or voltage LRC circuitry, then the

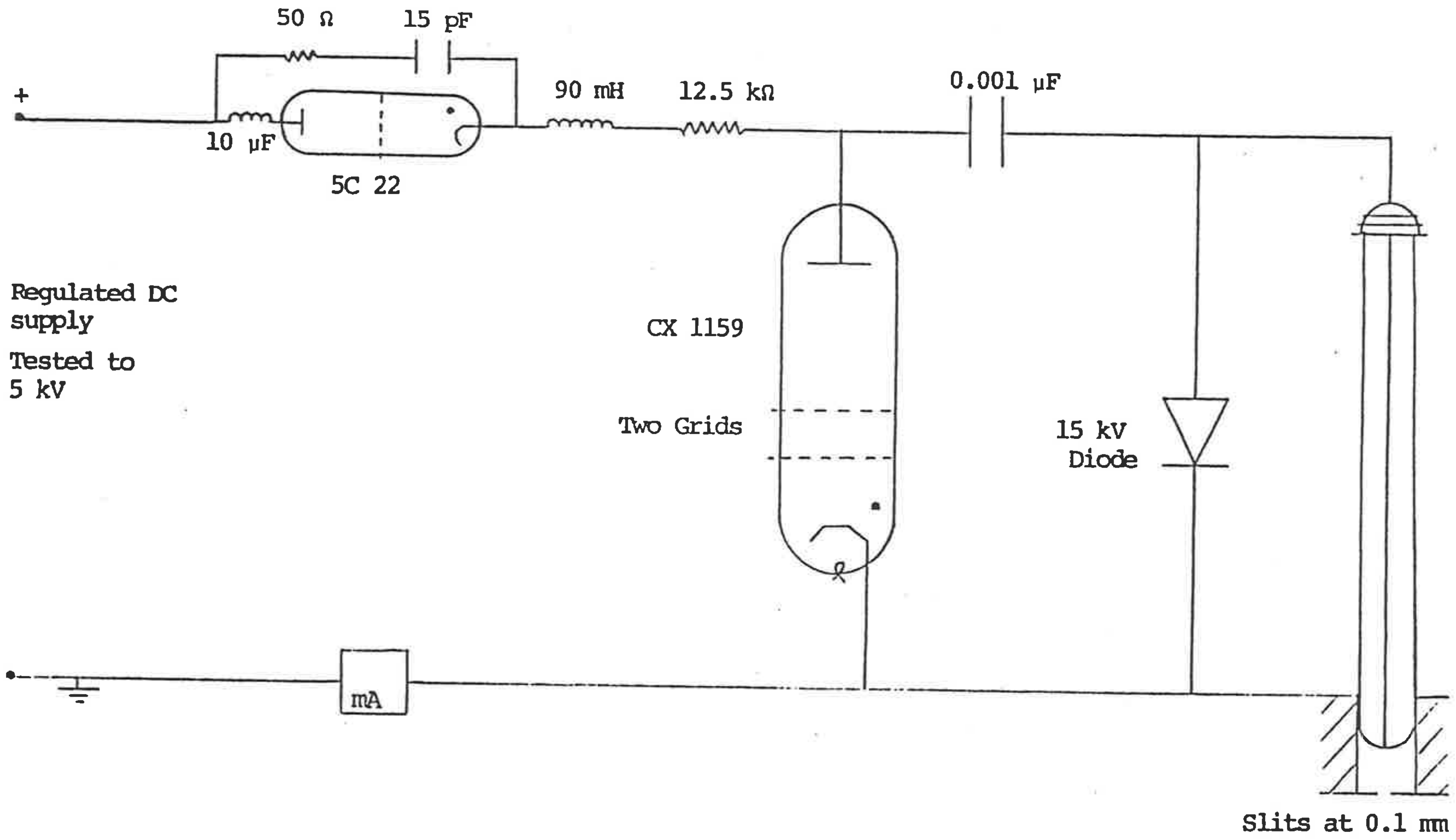

Figure II.4 Schematic of new pulsing circuitry, with floating thyratron in place.

thyratron may stay-on, drawing a continuous current limited only by the circuit resistance.

The solution, suggested by Dr McCoy, based on an idea from Merchant _et al_. (1978), is to ensure that the discharging thyratron is isolated from the power supply. This might be done, in theory, by the presence of a floating thyratron (Figure II.4) that is held open circuit as the lamp is pulsed, and remains so to allow time for the CX1159 to switch-off. Once this happens, the spark capacitor can be recharged via the 5C22. With the diode and small thyratron in line, the anode voltage is clamped at the peak in the LRC ringing, as little reversal of current is possible. And, similarly, sufficient time must be allowed for the 5C22 to switch off.

However, in spite of these safeguards, latching can still occur. Two mechanisms have been put forward, both resulting in the two thyratrons being closed concurrently. The critical moment is the high current density discharge through the CX1159. As the anode voltage rapidly drops, a grid pulse may be generated at the 5C22, due to stray capacitance. Alternatively, sufficient noise may be produced to cause a pulse in the triggering circuit, again firing the 5C22 out of sequence. The latter effect would appear to be more severe, as evidenced by the marked improvement in lamp stability, when the triggering supply is placed outside the noisy environment (a doubly shielded cage containing the main electronics).

There is a touch of irony here in that the charging circuit only works at high frequencies or, more specifically, high LRC ringing levels, as these are necessary to ensure the stable switch-on of the floating tube. If this is not the case, the 5C22 appears to go into an oscillating on-off state, enhancing the chances of both tubes being on simultaneously. For similar reasons, the pulsing frequency must be initially held low, as the supply voltage is first wound up. The small loop of LRC circuitry about the 5C22 also appears to aid in stability by providing a starting plasma on firing. Note that there is no longer any danger of the 5C22 overheating as peak instantaneous currents are greatly reduced. The CX1159's heating factor now sets the voltage/frequency limit.

The best results to date are 17kHz at 5kV. That should correspond to an increase in light flux by greater than 3, but this is yet to be ascertained as noise levels prohibit the computer collection of data. This disability is independent of frequency, arising only from noise generated in each current pulse. Importantly, this is not a matter of radiation, depending as it does on a physical connection to the computer interface. Possible problems are:

1) The peak voltage being discharged depends on the damping of resistors. But the current circuit would appear to be more greatly damped.

2) The diode, as opposed to a resistive inductor, could cause trouble with voltage overshoot, allowing high current pulses to pass, at least in one direction.

3) A less inductive thyratron would lead to a shorter intenser pulse. And thus, though brighter, a noisier lamp.

More important than reasons are solutions. Besides shielding in all the likely trouble spots, ferrite rings on the data lines have been suggested.

II.3 The Computer Interface

The idea of interfacing with a computer is to provide greater flexibility, and ease of handling, by software as opposed to 'hard-wired' control.

The computer interface is largely of a standard 37 pin design, allowing connection to a testing device in times of trouble. It provides us with address space for communication to and from the photoelectron system. The computer is a Commodore 4016 with high resolution graphics.

Two D.I.L. boards have been incorporated into the interface design. They are:

A) Retarding Voltage Board

Described more fully in Jones (1982), this involves a 16 bit D/A converter giving a controlled output current of remarkable stability. After further suitable conversion, an output voltage is produced, accurate to better than 1mV over a 20V range. Significantly, this voltage can now follow the inverse energy law with wavelength, once the computer is fed with the appropriate information.

B) Data Board

A little more detailing is warranted here, as this has not been described elsewhere. Figure II.5 presents a schematic view.

Three data ports and an advance wavelength line communicate with the outside world. The data lines can all be sampled concurrently, thus doing away with the

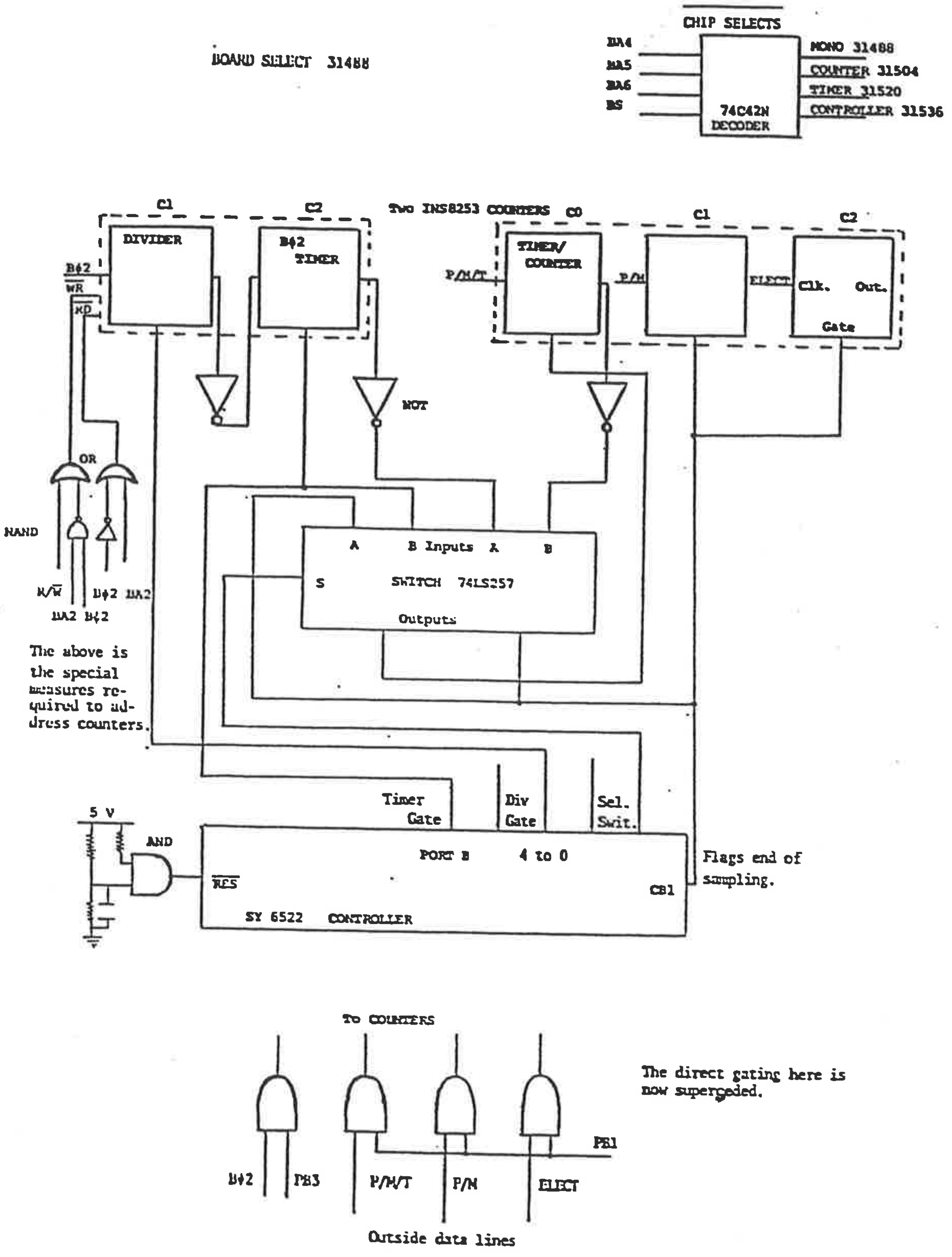

The above is the special measures required to address counters.

The direct gating here is now supergeded.

Figure II.5 Schematic of Data Board.

necessity of the electronically derived sum and difference (see Figure II.1); with both front and back photomultiplier signals always available, it is just simple arithmetic. However, the old ways may still be convenient.

Two methods of timing are possible.

a) Sampling for a fixed time, as measured by counting the buffered phase 2 clock from the CBM.

b) Sampling for a fixed number of data pulses, on the port marked P/M/T.

Three rather sophisticated programmable chips are on board. Firstly the SY6522. This acts as control headquarters, directing the necessary gating of data, and signalling to the CBM when sampling has finished.

The other two chips are IN8253 programmable interval timers. The 'one-shot mode' of timing is always used. There are two important features of these devices of which the reader should be aware. Firstly, they only show the correct count after they have received at least one pulse. This could present difficulties in low count rate experiments. Secondly, they tend to be rather sensitive to noise.

Table II.1 provides all the required information for any experimental set-up. To better understand this entire section the relevant data sheets should be consulted.

There is one last significant variable not being monitored by the computer. That is the pressure. This should at least be measured. Better still would be to have it fixed at a constant level. To allow for the complex, two-way device this would entail, a 77 pin rack has been installed in the interface.

Table II.1

Rundown of the various addresses for the proper deployment of the computer interface.

A = 31536: Rem Chip select for SY6522 controller chip.

B = 31520: Rem Chip select for timer chip.

C = 31504: Rem Chip select for counter chip.

D = 31488: Rem Chip select for monochromator wavelength advance.

E = 31744: Rem Chip select for retarding voltage supply.

Poke A+2,31: Rem Set direction of Port B's as outputs.

Poke A+0,8: Rem Switch set to timer mode-for P/M/T as timer (counter mode) poke in 9, and add 1 to all other data addressed to A+0.

Poke A+12,0: Rem CB1 set to be flagged on negative edge.

Poke C+7,48: Poke C+7,112: Poke C+7,176: Rem Mode 0 loaded to counters 0,1 & 2 respectively on the counter chip. The gate input inhibits counting when low.

Poke C+4,0: Poke C+4,0: Poke C+5,0: Poke C+5,0: Poke C+6,0: Poke C+6,0: Rem Counters 0,1 & 2 loaded with 0 - least significant byte first. Now ready for counting.

Poke B+7,116: Poke B+7,178: Rem Mode 2 to counter 1 and Mode 1 to counter 2 on timer chip. N.B. Mode 2 allows output to send one pulse to counter 2 after a certain number has been received by counter 1. A low gate inhibits counting. Mode 1 Output goes low on the count following the rising edge of the gate input - initiating count. The output goes high on the terminal count. When using P/M/T as timer simply Poke C+7,50.

Poke B+5,232: Poke B+5,3: Rem Divider (counter 1) loaded with 1000 - thus pulses counter 2 on timer chip every millisecond.

Poke B+6,100: Poke B+6,0: Rem Counter 2 on timer chip loaded with 100 - sampling for 0.1 seconds.

Poke E+1,VU: Poke E+2,VL: Poke E+0,0: Rem Load most significant then least significant byte into D/A converter. Then poke through to grid. A small delay might be in order here to allow time for voltage to settle.

Poke A+0,30: Rem Data collection begins. Strictly need only poke 19 with P/M/T as timer.

Wait A+13,16,0: Rem Detects end of count.

Poke D,0: T2=TI: Rem Advance monochromator at time T2.

Poke A+0,8: Rem Gates closed.

For P=0 to 2: F(P)=65536-Peek(C+P)-Peek(C+P): Next P: Rem Reading counters on the counter chip. Note that they are down counters.

If TI-T2 < 1.8*IC Then Goto (start of line): Rem Delay for wavelength advance. IC is the increment used.

Loop back for next channel.

CHAPTER III

III. THE ELECTRON ANALYSER

Although no modifications were made to this part of the equipment, nevertheless, as a key piece of apparatus in photoelectron work, it's behaviour should be understood in some detail.

To begin, a brief comparison is given of retarding and differential analysers, including a qualitative discussion of the limits of analyser performance and the reasons for choosing our particular model.

What follows is an annotated list of the various effects leading to the detailed integral spectral shape. As far as possible, this traces the path of an electron through the system from aperture to channeltron. Finally, all the effects are pieced together, to see what insights might be gained. Of particular concern is how the resolution and efficiency vary with energy.

III.1 Various Types Of Analyser

The particular analyser under study goes by the full title of a Spherical Retarding Potential Photoelectron Analyser. Figure III.1, reproduced here for your convenience, provides the relevant structural information. Throughout this chapter, and the next, the same nomenclature as Lindemans' is used. Most importantly the Earth grid becomes E, Retarding, R, Accelerating, A, and Focussing, F. With a computer controlled negative voltage applied to the R grid, the reason for the device name should be evident. Furthermore, assuming A and F have no other effect than to focus electrons on to the channeltron detector, the recorded signal should be the sum of electrons with energies greater than the retarding potential. Upon scanning of this potential, a typical integral spectrum results (Figure III.2a), with steps occurring as electrons arising from successive ionic levels are removed. The height of each step gives it's intensity, once allowance is made for detecting electrons of a given energy, that is, for the efficiency.

Looking through the literature though, the most common representation of photoelectron spectra is the differential or peaked curve (Figure III.2c), where the area under a peak relates to the intensity, again allowing for efficiency. These curves arise quite naturally for deflector or dispersive type analysers (Gardner and Samson, 1973), which only count electrons within a small energy window. They are also possible, after a fashion,

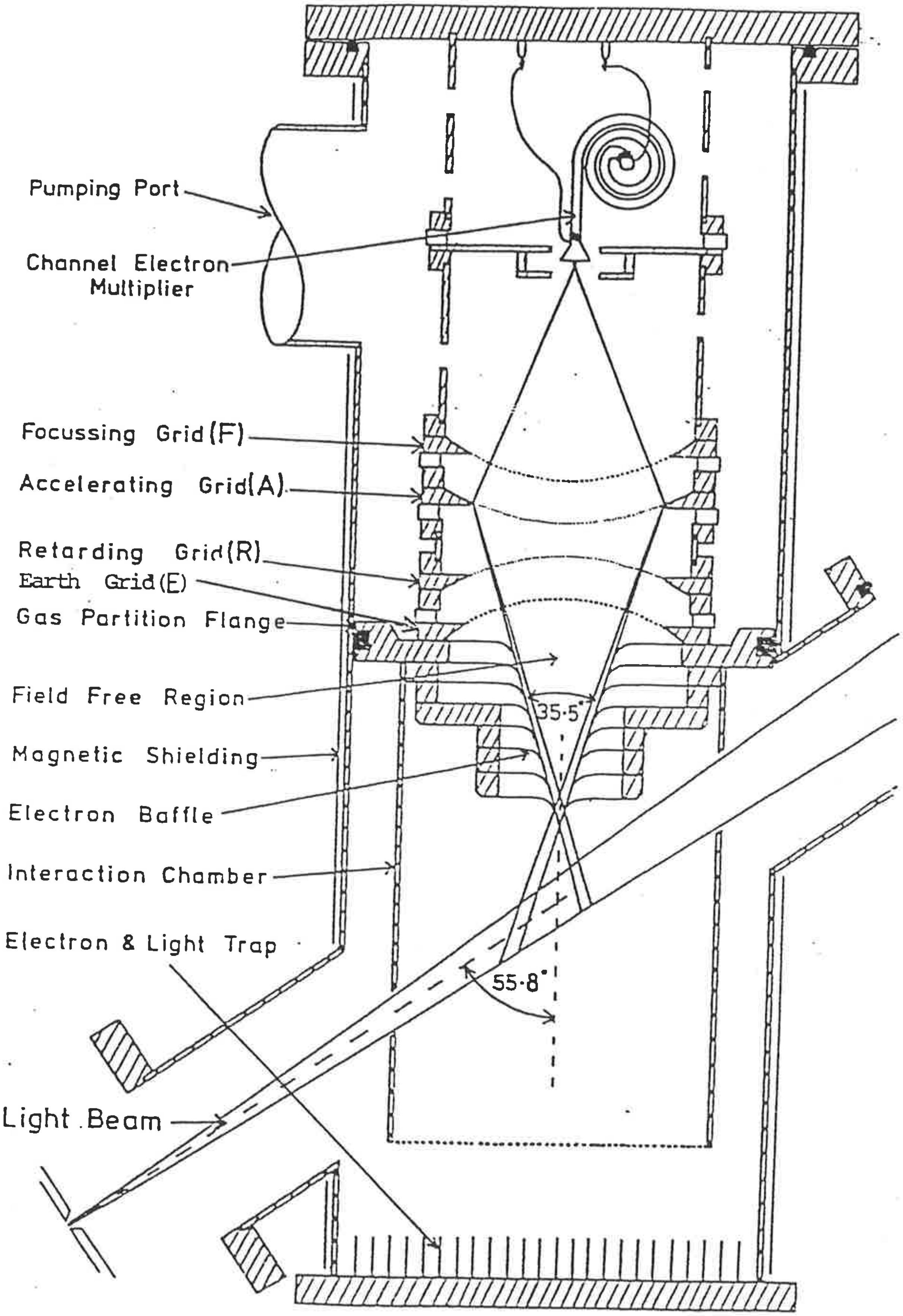

Figure III.1 Scale drawing of the Electron Analyser.

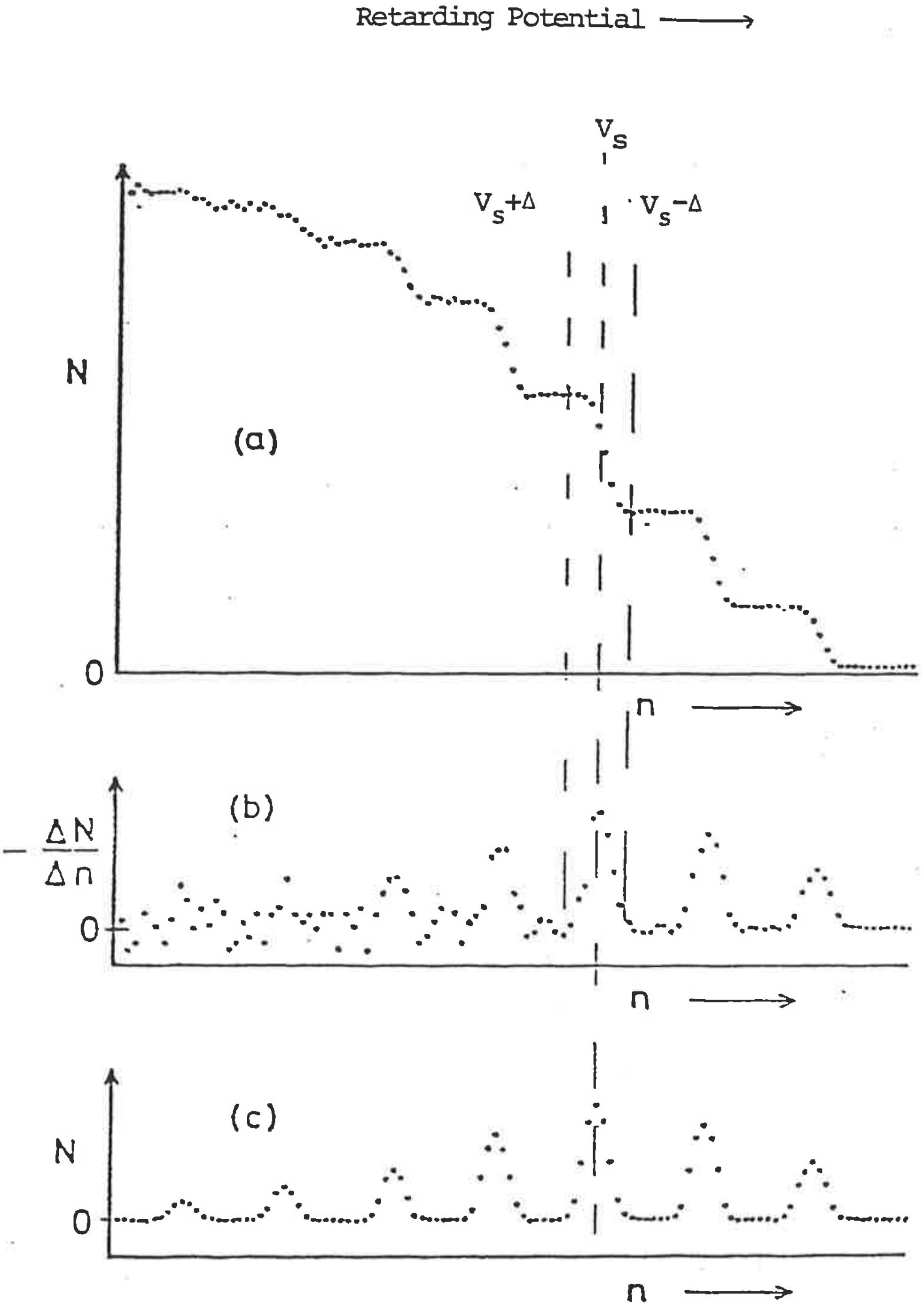

Figure III.2 Integral and differential photoelectron spectra. N and n represent the electron count and channels numbers respectively. Graph (a) shows a step spectrum from the retarding analyser, (b) the same spectrum differentiated, and (c) an idealised differential spectrum from a focussing spectrometer of the same resolution.

for retarding types (Figure III.2b), by introducing a square wave, of positive then negative volts, atop the scanning potential and counting up then down at each point. I say 'after a fashion', as each point still retains the integrated statistics or, more precisely, root 2 times them.

In the past, the large background associated with the higher levels in integral spectra has been cited as a reason for not using them. It is hoped that this thesis will show this to be largely unwarranted. For one thing, in the case of the lower vibrational levels of oxygen or nitrogen ions, with their typical spacings of 200meV, the easily attained resolution of 40meV ensures significantly more data points are available for intensity analysis in the integral as opposed to differential spectrum. This comes about since points between steps are of major importance in the height analysis.

There are several other differences between deflector and retarding analysers that should be mentioned. Most pertinent is that, for a given resolution, the retarding models have a far greater acceptance cone. This is negated only slightly by the reduced transmission due to grids. The resulting high count rate is just what is needed in relative intensity measurements. In fairness it must be stated that deflective instruments are capable of far superior resolution, making them ideal for energy level analysis. Indeed, the energy levels of Samson and Gardner (1977) are borrowed for our own data manipulations.

On the pro side, once again, our instrument is less sensitive to stray magnetic and electric fields. And finally, with it's efficiency such a simple function (see later in chapter), it requires less care in calibration than a deflective apparatus.

III.2 General Features of the Spectral Step

Any real spectrum can be roughly divided into 4 separate regions. Running from low to high retarding levels they are the plateau, peaking, edge and background (Fig. III.3). It is these regions that must be explained. In particular, the step edge has an associated resolution and shift, both dependent on electron energy. And how does one determine the exact height of a step, when the plateau is not strictly flat?

III.2.1a Grid Effects

Grids are not the ideal retarding system, just the simplest and the best (for our basic design). Their problems arise largely through finite transparency and imperfect potential surfaces. When you realise that field lines must arrive at right angles to the wire surfaces, it is easy to see that complex fields occur. For low energy electrons this can result in severe deflections as they approach a grid. These might conveniently be termed lens effects, in analogy to refraction in optical lenses. Furthermore, the average potential in the 'plane' of the grid surface differs from that applied. For want of a better name, these may be simply termed shift effects. The significance of both these effects is in direct proportion to the field strengths involved, which are generally strongest along the axis of the analyser (for R and A).

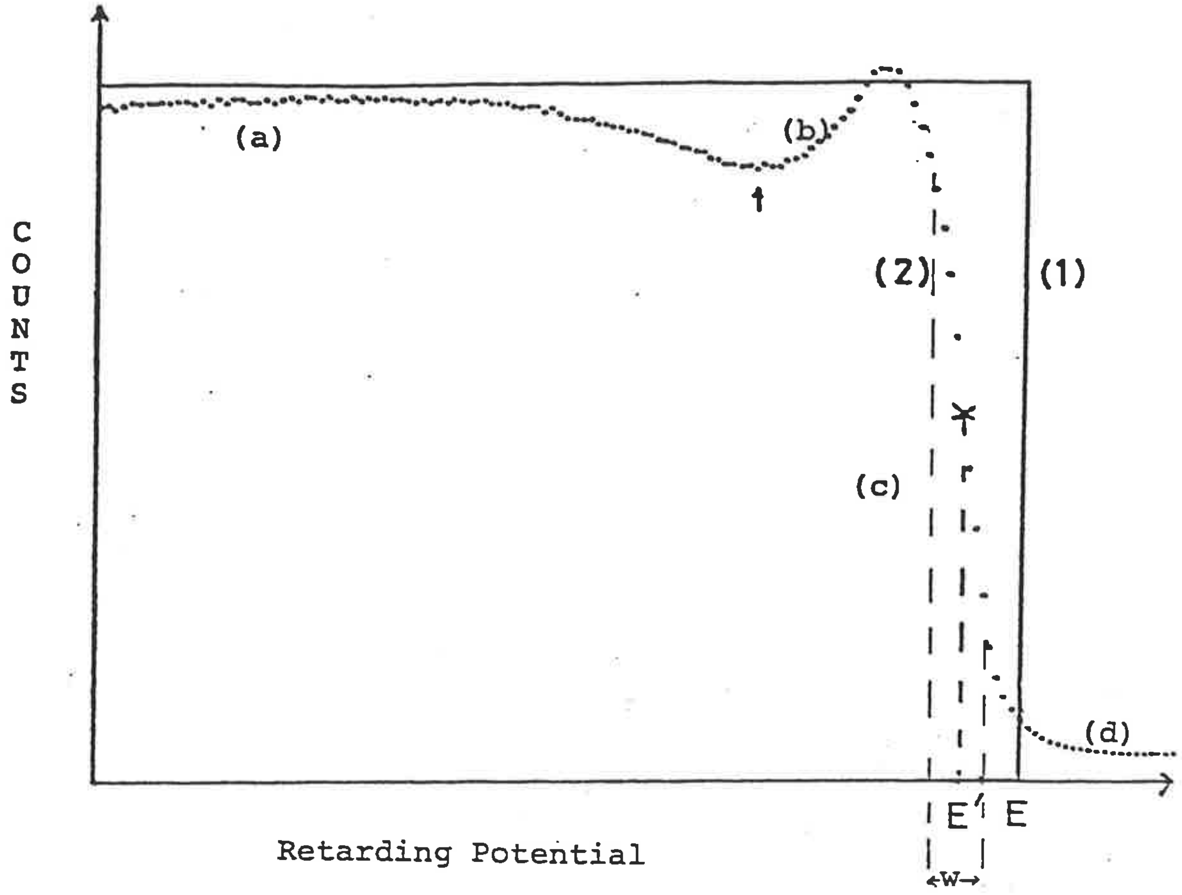

Figure III.3 Ideal and experimental integral energy spectra. The ideal curve (1) shows a sudden change in count at energy E, the electron energy.
The experimental curve (2) can be roughly divided into 4 parts.

(a) The plateau, well away from the step.
(b) The peaking region, exaggerated here, occurs near the step and makes the step height estimate difficult.
(c) The step edge. This should strictly be divided into a low and high energy tail as these arise from separate effects.
(d) The background.

NB The "valley" between plateau and peaking, as arrowed, is important for height estimation.

The step centre generally occurs at an energy other than the true electron energy, thus giving a shift=E-E'.

The step width, w, is measured with respect to the 20% & 80% peak height points.

III.2.1b Stray Magnetic and Electric Effects

In the presence of the Earth's magnetic field a photoelectron follows a curved path, without any change in it's speed. Thus as the electron enters the region between the E and R grids, it becomes misaligned with the radial electric field, causing an effective drop in the absolute stopping potential. In fact, there is both a shift and spread in this potential, as the magnetic field is highly non-uniform with respect to the electron paths. It has been shown in Lindemans App. I (1981) that this shift and spread is independent of the initial electron energy. But the result is still a severely degraded spectrum. Appropriate shielding fortunately reduces the field to a more tolerable level, ensuring adequate resolution.

However, over a period of months, with the constant vibration of the extensive pumping, the shielding material, itself, becomes magnetised, leading to a progressive worsening of results, and the eventual need for degaussing (Lindemans, 1981, p.57).

The main concern with stray electric fields is the variation in contact potential due to oil vapour deposited on the grids (Parker and Warren, 1962), again degrading the step response. With time this steadily becomes worse, as the UV bombardment causes a breakdown of the silicone based oils into worse by-products, which finally necessitates a trichloro ethylene vapour bath, starting the process all over again (Lindemans, 1981, p.54). Note that the effect on resolution and shift would appear to be linear with electron energy.

From the two above effects, it can be seen that the analyser response is not a constant with time - that the system 'ages'. Given this, it should be clear that finding the step function is not a one-shot process, but must be done repeatedly, making a simple technique all the more desirable.

Table III.1 now summarises the various individual effects. For a more thorough treatment Lindemans (1981) Ch. III should be consulted.

TABLE III.1: VARIOUS EFFECTS LEADING TO STEP PROFILE

Grid Region	Step Region	Comments	Size of Effect
E	Plateau	The largely elastic collisions lead to a linear correlation with energy.	2.5% plateau at $V_r=0$ atop step.
Between E & R	Edge	Electron paths should be parallel with radial field. However, due to: a) Finite size of source and aperture, electrons enter region at a variety of angles - unavoidable. b) Limitations to exact construction lead to slightly non-radial fields. c) Magnetic fields curve path of electron.	a) Width=1.6 mV/V plus similar shift. b) W=2 mV/V plus similar shift. c) Constant shift and width for any energy.
R	Peaking and Edge	a) Lens effects lead to electron paths avoiding wires as V_r approaches electron energy, e, thus passing through and adding to count. But as V_r more nearly approaches e, a stage is reached where deflections lead to failure to penetrate the retarding barrier. b) Shift effects give rise to a higher than expected step centre energy. In fact, the electron will experience a range of altered, potentials depending on it's exact path through the system. c) Oil film alters the retarding potential seen by the electron.	a) Peaking linearly dependent on energy. Spread 2.5 mV/V b) Shift to higher energy 2.3 mV/V plus similar spread. c) Shift and spread approximately linearly related to e.
A	Peaking	Lens effects lead to peaking.	Acc. field is .1 V_r.
F	Plateau	Imperfect focussing for electron arriving at R with sufficient energy.	For V_f of 500 V, an electron with greater than 2eV energy at R is poorly focussed.
Channeltron		No efficiency effects as electron arrives with a virtually constant 500eV of energy.	Applies for electron with less than 20eV initial energy.

III.2.2 The Sum of the Various Effects

The discussion below follows the four step elements, from low to high retarding potentials. Repeated referral to Table III.1 is recommended.

A) The Plateau (Figure III.4a)

The poor focussing by the F grid ruins the strictly linear scaling of the plateau shape with electron energy, from scattering off E. However, for any segment of plateau within 2V of the step edge, linearity holds true. One might be tempted to raise the F voltage to 1000V to rule out defocussing (Lindemans, 1981, p.102), but this would be at the expense of enhanced peaking.

B) The Peaking (Figure III.4b)

Combining effects from the R and A grids, this should be largely linearly scaled with electron energy, but for the step edge eating into this region. A little consideration suggests an enhanced peaking at higher energies (see C) The Edge).

C) The Edge (Figure III.4c)

Finding the resolution is not a simple matter of adding Gaussian widths, like so

$$W_{Total} = \sqrt{W_m^2 + W_g^2 + \ldots} \qquad \text{III.1}$$

even if the edge can be approximated to an integrated Gaussian. This is so because the various effects (magnetic, geometric etc.) do not work independently, but

Figure III.4 Successive finer detailing of two integral steps, one of high energy (.), one of low (-). Effects that scale linearly with absolute step centre potential (∿electron energy) can be shown up by normalising the step centre potential to -1: i.e. steps are over the same distance on the x-axis.

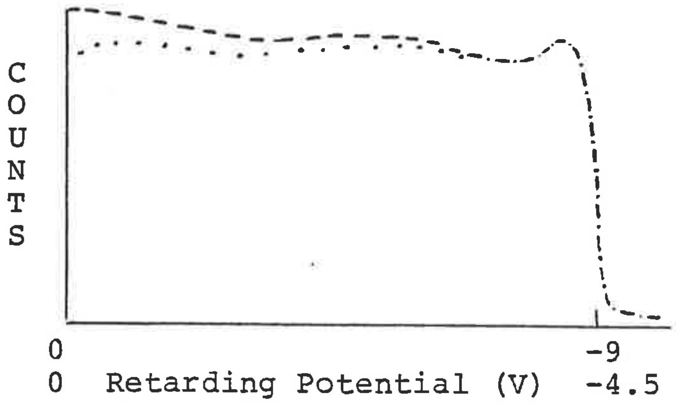

(a) Plateau effects are strictly linear only within 2 eV of the step.

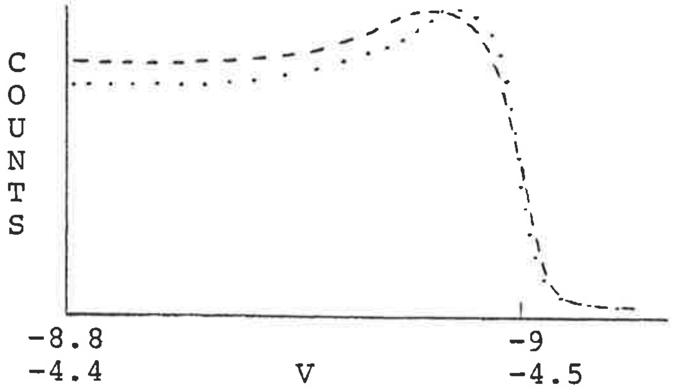

(b) Higher energy means enhanced peaking?

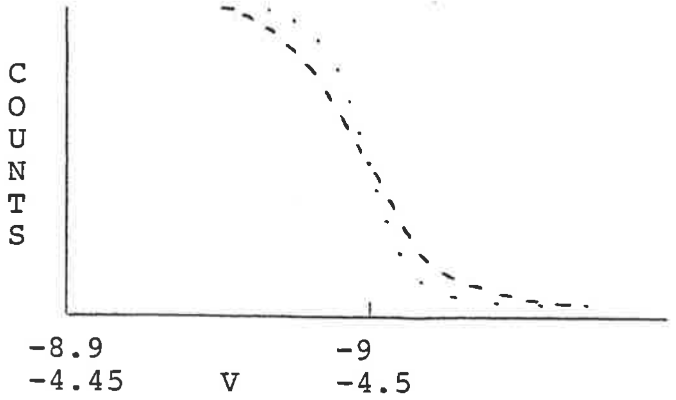

(c) Generally the width doesn't scale linearly with energy.

NB The above voltage ranges aren't to be taken too seriously. This page is only meant as a qualitative guide.

must be combined in a complicated integration to obtain the summed result. No attempt will be made to do that here.

One point that should be clear: depending on how dominant the constant magnetic effect is, the weaker the variation of width with energy will be. All other effects should tend toward a linear relation between energy and width (or related inverse slope). Similar behaviour can be expected from the step shift.

D) The Background

Though only seen as a high energy tail in Figure III.3, it adds to the count at all potentials. It contains wall photoelectrons, degraded gas photoelectrons (those that have undergone collisions with the walls and lost their original energy), detector noise and scattered photons. The final two add a constant level, independent of retarding voltage.

One last feature needs to be accounted for - the step height. The region between plateau and peaking is a shallow 'valley', the position of which is approximately linearly scaled to step potential. As it is always within 2V of the step edge, at least for electron energies less than 10eV, no defocussing effects are involved. Thus the step height here simply corresponds to the transparency level of the analyser. This remains true, but for low energy electrons, for which the plateau and peaking regions merge, adding to the detected count relative to the transparency level. Finally, for the very lowest energies of the order of the width of the step edge, the valley level will drop off dramatically. From this discussion an efficiency curve can be constructed for detecting valley electrons (Figure III.5).

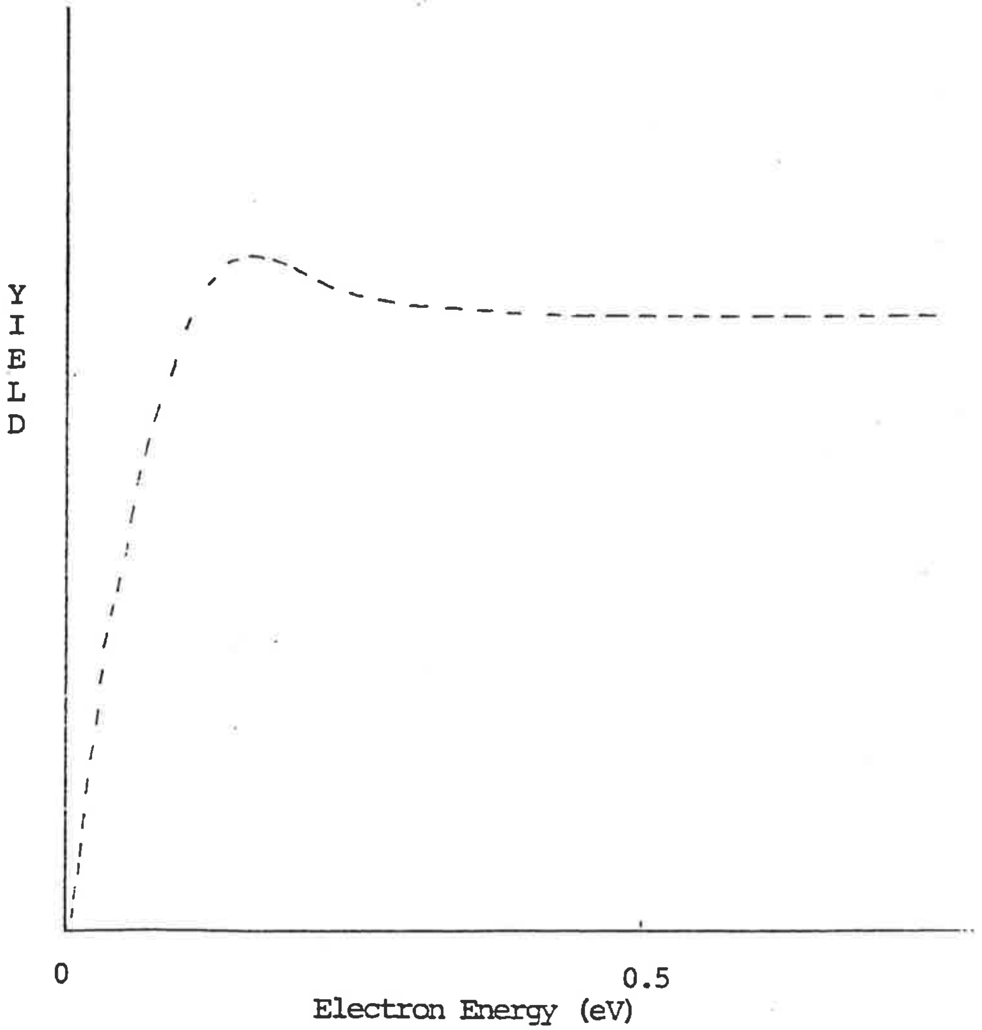

Figure III.5 Probable efficiency function measured with respect to the valley of an integral step. The yield is a measure of the number of electrons detected per photon absorbed. Ideally the yield for an Inert gas in the energy range of interest should be constant.

CHAPTER IV

IV. CURVE FITTING AND PHOTOELECTRON SPECTRA

Using Rare gases and two UV line sources, a small set of single steps at various energies is obtained. These steps are shown to be well representative of the instrumental response of the analyser, nearly independent of the particular gas used. Now the question is, can these few curves be employed to find the step shape at an arbitrary energy of interest? To this end, two distinct curve fitting routines, functional and numerical, are developed and their relative merits investigated.

Then there is a quantitative treatment of the efficiency function to allow correct determination of the step height. This is of major concern for obtaining accurate branching ratios in Chapter V.

All this work is backed up by the detailed understanding of the electron analyser gained in Chapter III.

IV.1 Experimental Procedure

The first step in any quantitative description of the analyser response function is the collection of a representative set of monoenergetic curves. The Inert gas spectra, notably krypton and xenon, with their widely separated spin-orbit components and their exceptional cross-sections, are the natural choice. Also argon, with it's relatively close components, can be largely treated as a single step, when looking for plateau effects. The only non-instrumental contributions to the step spread are those discussed by Turner (1968) for atomic gases. The most significant of these at room temperature results from the thermal velocity of the target atom; from $v_a = (3kT/M)^{\frac{1}{2}}$, where M is the mass of the atom. This introduces a typical velocity error of $2v_a/\sqrt{2}$ on top of the electron velocity, v_e. (Consider the extreme case of two atoms moving in opposite directions. The $1/\sqrt{2}$ averages the result.) To obtain the resultant electron energy spread, you must differentiate the kinetic energy relation.

$$dE = \tfrac{1}{2}m \; 2v_e dv_e \qquad \text{IV.1}$$

Two simple substitutions then lead to the desired equation.

$$\Delta E = \left(\frac{12\,E\,k\,T\,m}{M} \right)^{\frac{1}{2}} \qquad \text{IV.2}$$

For argon at 10eV, this rather awkward energy variation amounts to a 6.5meV spread, compared with about 35meV for instrumental effects. And the non-linear addition, as of Equation III.1, further ensures the larger effect dominates. Therefore, such effects will be ignored in our considerations.

The chosen UV sources are two of the brightest atomic lines, namely HeI 58.4nm and NeI 73.6nm. This gives a range of curves from about 0.9 to 9eV, more than adequate for finding any energy variation.

The Inert gas spectra were all recorded under controlled experimental conditions. The same applies to all future efforts.

1) There must be at least 24 hours of continuous diffusion pumping of both the monochromator and table (contains analyser and ionisation region), before any data is taken. This ensures the system reaches some sort of equilibrium. Notably, molecules not outgassed from the channeltron are readily ionised by it when on, leading to erratic response.

   In the early stages of pump down, both table pumps may be employed but the differential pumping (across face of analyser) is unnecessary during data collection. Liquid air is absolutely imperative, for both pumps, in reducing water and oil vapour contaminations. As mentioned earlier, the analyser is particularly sensitive to oil.

2) The photomultipliers are switched on an hour (or two after a long lay off) before the experiment. There is a distinct tendency for the dark count to monotonically decrease, leading to a good deal of offsetting. Only the back tube is warranted, when sitting at one wavelength, giving an extra 20% of UV light, once the beam splitter is swung out the way. It is worth

remembering that the count statistics should be considerably better than Poisson, with the tube in current mode.

For bright UV sources the tube gain is lowered by a reduced power supply voltage. Optimum linearity is guaranteed with a 120kHz signal or thereabouts.

3) The UV source may take a ½ hour to settle, particularly if impurities have not been outgassed or flushed out.

4) The D/A staircase voltage supply needs just 15 minutes 'oven' time.

5) When using a line source, ensure no other lines contribute significantly via a wavelength scan and adjustment of the exit slit. (This is particularly important for the NeI pair, 73.6 and 74.4nm.) Pressure broadening may also be tested by repeated scanning and comparison of line profiles, as the lamp pressure is altered. Both these effects can lead to a highly non-monochromatic source giving a false instrumental analyser response.

With the UV source blazing, the photomultiplier is further offset to the scattered light background (Lindemans, 1981, p.133). A 50nm wavelength setting is typically used. Then rescan for the desired wavelength.

6) The channeltron needs no warm-up. The only precaution to be heeded is that it is not on with the pressure in the ionisation region exceeding 1.5mT (Pirani gauge), or voltage breakdown will surely follow.

7) A background spectrum is first recorded ('no' gas in the ionisation region) over an equivalent voltage range to the main scan, but with a submultiple of channels (N.B. There is always a zero channel.) This aids in future analysis. A detailed mapping of the energy variation is not necessary with absence of an inherent background structure. Any steps here are probably indicative of a leak, but this should show up on the ionisation gauge.

Now, once inlet lines have been flushed, in the case of high pressure supplies, or pumped out for the xenon and krypton one-litre flasks, the gas is introduced at the desired pressure. This can take a while to settle, and still tends to drift down during an experiment. However, repeated cycling through the voltage range counters this.

At this point the lamp intensity may have to be reduced, to guard against pulse count saturation and pulse coincidence effects, for DC and pulsed sources respectively (Lindemans, 1981, p.117). In any event step 5 must be repeated as the scattered light level changes in the presence of gas.

An extra measure yet to be tested is the reversal of staircase* scanning on alternate cycles, avoiding anomalous fluctuations in channeltron gain when switching from small (tail) to large (plateau) count rates in a single bound (Lindemans, 1981, p.117).

---

* Referring to the stepwise fashion of voltage increments for each channel.

Something else that has not been done this time round is the recording of the photon background with and without gas present. This is seen as a small but constant count rate when the retarding voltage is set to a level approaching the UV photon's energy. Unfortunately, the required voltage cannot currently be obtained without some offsetting or rescaling of the staircase. The error introduced by it's neglect, however, is minor.

The optimal 'cell' pressure is still a matter of some controversy. If the atomic scattering cross-section is large for electrons, particularly those of low energy, there is a tendency to round off the step (Lindemans, 1981, p.123). Thus the pressure must be reduced until no change in step shape is discernable. This can be done quantitatively by looking for a value of about one in the following.

$$\sum_i \frac{(Y_{1\,i}^{-} - aY_{2\,i}^{-})^2}{(Y_{1\,i} + a^2 Y_{2\,i})N} \qquad \text{IV.3}$$

i is the channel number: same channel, equivalent voltage.

- superscript means background subtracted.

1 and 2 subscripts refer to two independent sets of data, recorded at different pressures but over the same voltage range.

N is the number of data points.

The part of the denominator in brackets is equivalent to the square of the average difference between corresponding data points, provided the step shapes are equivalent. Thus each element of the sum would have a typical value of 1/N, leading to the hoped-for total of one. Of course the value of a, which scales the two steps to the same height, must first be evaluated.

$$a = \sum_{i} Y_{1}\,\bar{i} \;/\; \Sigma \,.\, Y_{2i}\cdot \;\bar{\ } \qquad \text{IV.4}$$

To better understand the equations, consult the next section.

Current pressures employed are slightly lower than those of Lindemans' (see below). It should be emphasized that these are not absolutes but dependent on wavelength or, strictly speaking, the resultant electron energy (Frost et al., 1964).

TABLE IV.1: COMPARISON OF PRESSURES USED FOR VARIOUS GASES

	Lindemans (1981)	Present Work
Xenon	0.2 mT	0.17 mT
Krypton	0.4 mT	0.35 mT
Argon	0.7 mT	0.45 mT
Oxygen	1 mT	1 mT

IV.2 Some General Points About Curve Fitting

Throughout this chapter and the next considerable use is made of that powerful computing technique known as curve fitting. Already with Equation IV.3 the method has almost unwittingly been employed.

Take a typical photoelectron spectrum in Figure IV.1, consisting of 250 channels. For every data point there is a well defined retarding potential, x_i, and a statistically fluctuating count , y_i. Strictly speaking, these fluctuations will follow a Poisson distribution. But for counts of several hundreds or greater, a Gaussian approximation is more than adequate. Thus the following applies. From Chapter III and from the evident shape we can expect the true count to follow some continuous smooth function of x:

$$y(x) = f(x , \underline{a}) \qquad \text{IV.5}$$

where $\underline{a}$ represents a set of variable parameters, a_j, for j from o to n. To obtain the most likely final functional form, we must minimise the following with respect to each of the parameters.

$$\chi^2 = \sum_i \left[\frac{1}{\sigma_i^2} (y_i - f(x , \underline{a}))^2 \right] \qquad \text{IV.6}$$

where χ^2 is a measure of the goodness of fit. This is the Method of Weighted Least Squares. The only unknowns here are the standard deviations of each data point, σ_i. The square roots of the data are the best available estimates of these.

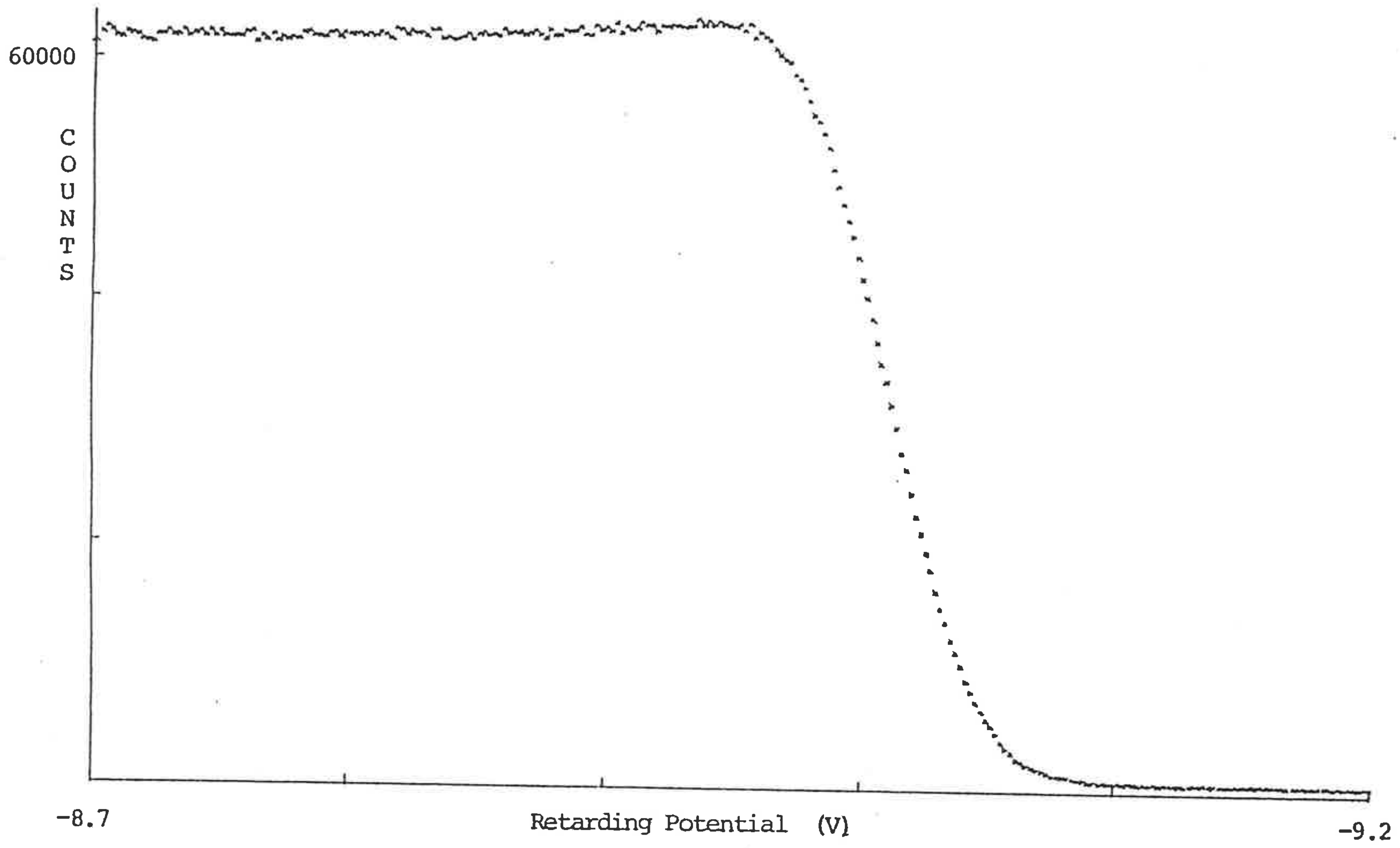

Figure IV.1 Raw data of the lower step for xenon, recorded using the 58.4 nm helium line.

Minimisation is achieved by setting the partial derivatives of each parameter to 0, giving a set of n+1 equations. If f has the form

$$f(x) = a_0\ X_0(x) + a_1\ X_1(x) + a_2\ X_2(x) + \ldots + a_n\ X_n(x) \qquad \text{IV.7}$$

a matrix equation can be formulated and it's solution found - the most likely values of each a_j - by a single matrix inversion. For the more general case of a non-linear function, a single inversion does not suffice. Rather, a complicated search routine is required, as is well documented by Lindemans (1981, p.168). But in both cases the inverted matrix contains all the error information, that is, Δa_j (Bevington, p.242).

Looking back at Equation IV.6, it should be apparent that each element of the sum averages a value of about one, if f follows a smooth curve 'through' the data. This leads to the more appropriate reduced χ^2.

$$\text{red.}\ \chi^2 = \chi^2/(N-\nu) \qquad \text{IV.8}$$

N : number of independent data points
ν : number of variable parameters = n+1

$N-\nu$ equals the number of degrees of freedom. The chances of exceeding various values of red.χ^2 for a given number of degrees of freedom is also well documented (Bevington App. C.4). For a red. $\chi^2 = 1$, it is generally about 50%.

For a more complete coverage of this section, Bevington (1969) is essential reading.

IV.2.1 A Functional Fit

This is the method originally put forward by Lindemans. No attempt is made to derive the exact analyser function. Section III.2.2 indicated this to be rather difficult. And with the analyser's sensitivity to oil, the detailed functional form could alter drastically from month to month. Instead the known behaviour is mimicked by a set of appropriately added Fermi-Dirac steps.

$$F(x) = 1 / (1 + \exp(x)) \qquad \text{IV.9}$$

Table IV.2 presents the four steps and the 16 parameters involved. Together with Lindemans (1981) Fig V.10, this should make it clear how they are applied. Note also that due to the nature of the function, a complex non-linear fit is involved.

TABLE IV.2: A FUNCTIONAL APPROACH TO FITTING INTEGRAL STEP SPECTRA

The Total Step

$S(V)=a_1(F(X_1)+a_{11}F(X_2))(F(X_3)+a_6F(X_4)) + a_{10}\,B(V) +$ photon background

where $B(V)$ is the appropriate background curve.

The Step Elements

1) the step edge

$$X_1=4*a_3*(D+a_4D^2+a_5D^3)$$

2) scattered electrons in plateau

$$X_2=4*a_{12}*(D/E+a_{13})$$

3) focussing correction in plateau

$$X_3=-4*a_{14}*(D_1+a_{16}D_1^3)$$

4) lens effect resulting in peaking

$$X_4=4*a_7*D_2^2$$

where $D=V-E+a_2$, $D_1=D+a_{15}$, $D_2=D+a_8$ and E is the electron energy.

The Step Parameters

a_1	the step height
a_2	the step centre shift
a_3	the reduced step centre slope
a_4	the asymmetry of step edge
a_5	the linearity of the step edge
a_6	the height of the peaking
a_7	the width of the peaking
a_8	the position of the peaking
a_9	the asymmetry of the peaking - unassigned here
a_{10}	scales background
a_{11}	the size of the scattered electron plateau
a_{12}	the width of the scattered electron plateau
a_{13}	the position of the scattered electron plateau
a_{14}	the width of the defocussed region
a_{15}	the position of the defocussed region
a_{16}	the linearity of the defocussed region

And the end result of all this is a rather poor fit. Reduced χ^2's of 1.9 down to 1.5, as you go from the high to the low energy curves, where the peaking becomes more evident. The chances of getting a worse fit with a supposedly good function, are less than one in a thousand. This suggests the need for more parameters, so the curve can be followed more closely, thus adding to an already exorbitant number. And I have yet to introduce extra parameters to trace the energy variation; say aE+b for a_3, the step slope.

Of course this is not the only possible function. Indeed a skewed gaussian replacing $F(X_4)$, the peaking, produces a far better fit. However, it does not overcome the basically undesirable fact of a complex procedure that will not bear repeating too often as the system ages (Section III.2.1b). Something simpler is needed, which provides the impetus for a numerical fit.

IV.2.2 A Numerical Fit

The following is a refinement of the method first worked on by Hutton (1981). The reason why Lindemans chose to avoid this type of fit was the difficulty in interpolating between curves of different energy (Lindemans, 1981, p.166), with the few curves we have available. Laying two curves atop one another, with their step centres and 'heights' matched, readily shows this by the number of crossings. But these crossings can be largely overcome by appropriate energy scaling and making use of some of the theoretical ideas of Chapter III.

Basically, a curve is divided into the same 4 segments as in Section III.2

A) The Background

The background scan is first smoothed and interpolated to match the number of main scan channels.* The often repeated smoothing techniques are described more fully in Appendix I, together with other mathematical procedures used throughout this chapter. The corresponding constant photon levels are now subtracted from both the background and the step. At this stage the background may be scaled to the relevant tail section of the step, by looking for a reduced χ^2 of about 1, and then subtracted. It is important that sufficient background tail data points are included in any gas run to obtain an accurate fit. The scaling factor, a, is found by setting the partial derivative of χ^2 with respect to a to 0.

$$\chi^2 = \sum_i \frac{(S_i^- - a\,B_{si}^-)^2}{S_i} \qquad \text{IV.10}$$

S : main scan data
$-$ superscript: photon background subtracted
s subscript : smoothed data
i subscript : channel number in tail region.

(Note that B_{si} does not contribute significantly to the error as it has been smoothed: cf. Equation IV.3.) This gives

$$a = \sum_i \frac{S_i^-\,B_{si}^-}{S_i} \Bigg/ \sum_i \frac{{B_{si}^-}^2}{S_i} \qquad \text{IV.11}$$

---

* Hence the desire for a submultiple of channels in Section IV.1.

We are left with a raw step curve, $S_{\bar{j}} - a\,B_{s\bar{j}}$ for j running through all recorded channels, whose shape depends solely on photoelectrons from the gas under study. This is essentially the monoenergetic step we wanted. Importantly the statistics are still contained in the original data.

B) The Edge

The slopes and shifts at the step centres of each of the 'tailless' curves are measured by fitting a cubic and adjusting the number of channels to obtain a red. χ^2 of about 1 (Appendix I). This is with a view to matching the slopes by appropriate potential (x-axis) scaling. The step centres and slopes of interest correspond to the points of 0 curvature in the cubics, provided the appropriate channel ranges are chosen. The slopes must further be normalised to the height at the peak turning point. Note that this is not the same as the height used in branching ratio calculations.

Figure IV.2 presents the slope measurements graphically. A weak function with step centre energy is suggested. This is indicative of a predominant magnetic effect, which will not always be the case under different operating conditions; say greater use of the UV lamp, over a period of months preceding measurement (Section III.2.1b). Now taking two of the more widely separated curves and matching the slopes, peak heights, and step centres (Appendix I - interpolation), a remarkable likeness is found (Figure IV.3). This prompts the idea of a mother curve that could generate a step at any energy by

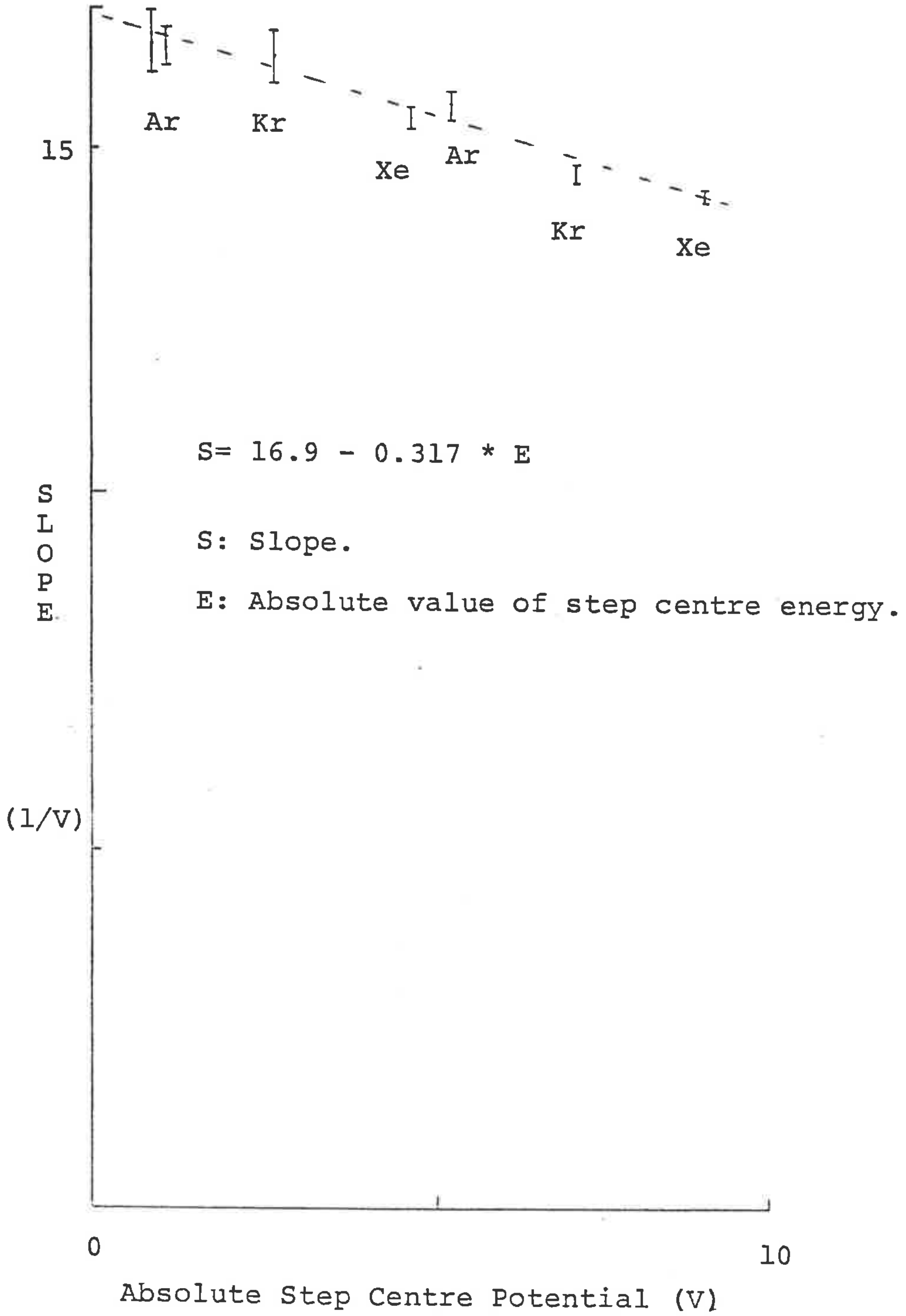

Figure IV.2 Relating the normalised slope to the step centre potential. Approximate error bars are from the cubic fitting routine. Theory suggests a strictly monotonic decrease in slope with increasing absolute potential. The dotted curve provides a reasonable straight line fit in accord with theory.

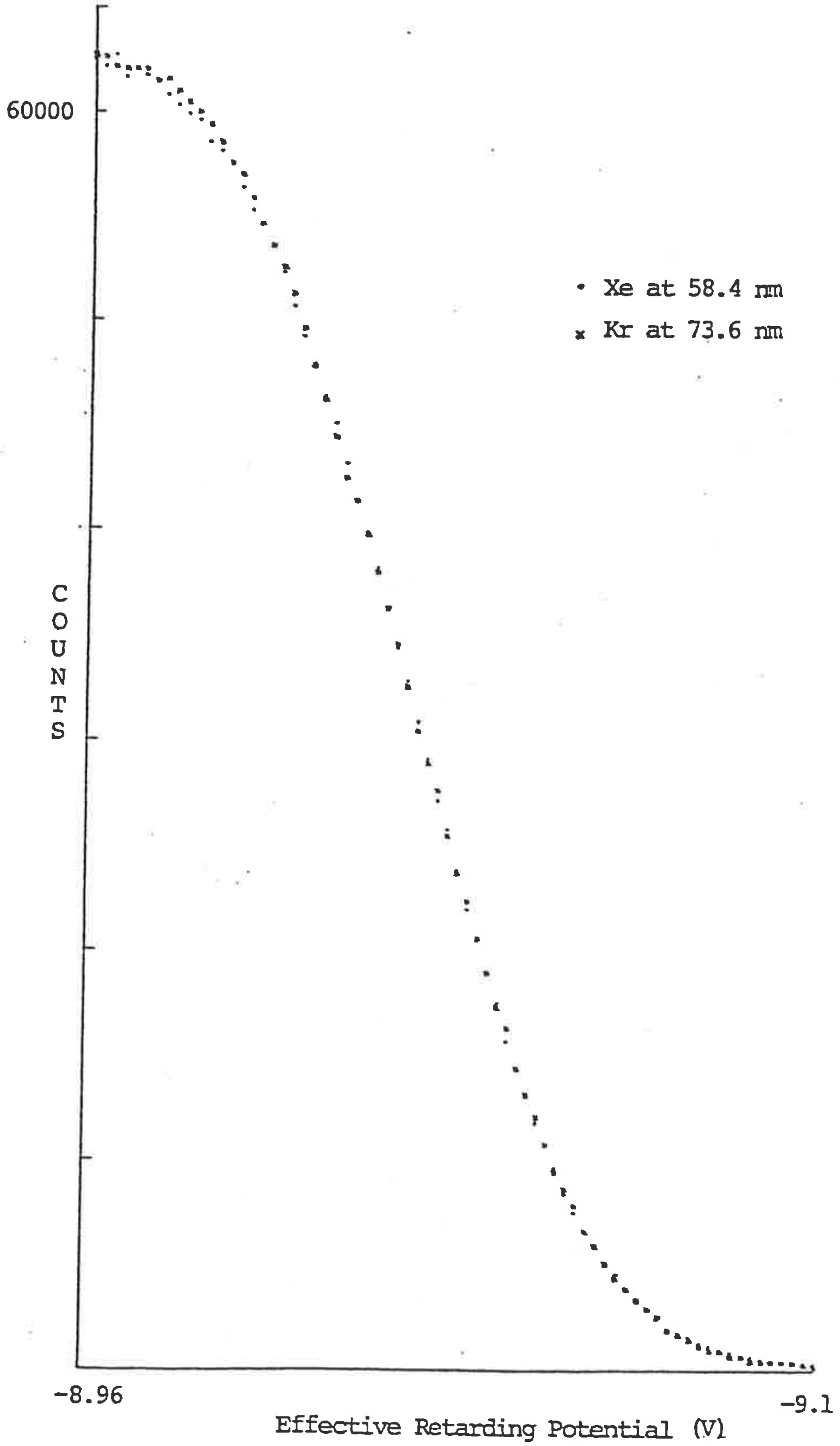

Figure IV.3 Match-up of step edges after krypton has been appropriately scaled to match step centre slope and position and peak turning point height.

the simple slope/energy relation of Figure IV.2. The closely mapped xenon 58.4 step is chosen for the task, after smoothing.

The other important parameter, the shift, shows an even weaker energy variation (Figure IV.4), again demonstrating the prevalence of magnetic effects. Table IV.3 provides the necessary information to make these measurements.

TABLE IV.3

The electron energies for the various Rare gas steps. A comparison with the step centre energies gives the shifts.

At 58.4 nm	Gas	eV
	Xe	9.088
	Kr	7.218
	Ar	5.458 ($P_{\frac{3}{2}}$)
		5.281 ($P_{\frac{1}{2}}$)
At 73.6 nm	Xe	4.718
	Kr	2.848
	Ar	1.088
		0.911

C) The Peaking

Section III.2.2 suggests a near linear scaling with energy for this feature of the curve, with possible problems for low energy electrons. Figure IV.5 presents the peaking difference between two 'low energy' curves and the mother curve, after appropriate scaling to the step centre potentials and the matching of the maximum turning points. Clearly the energy correlation is not perfect, else the

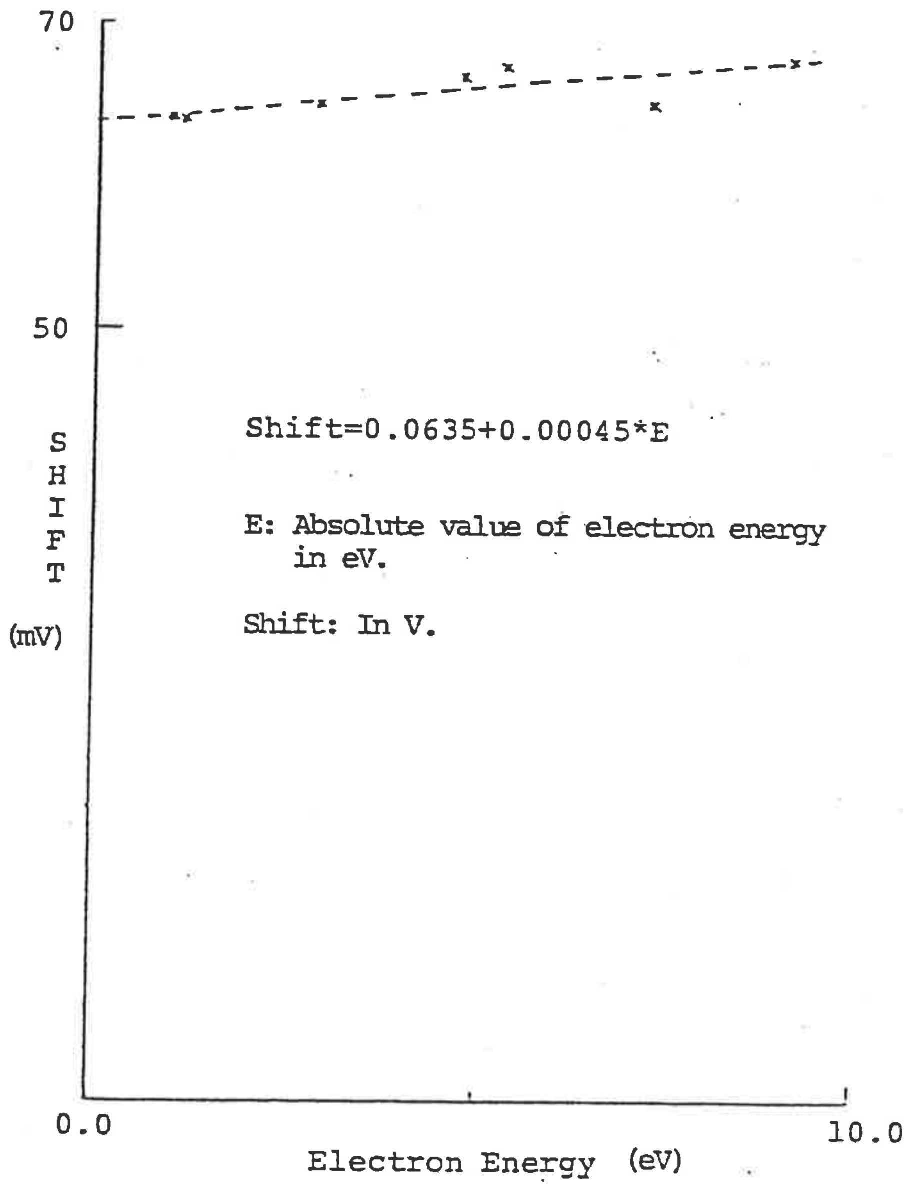

Figure IV.4 Variation of step centre shift with true electron energy. A positive shift corresponds to a displacement to the left on Figure IV.1.

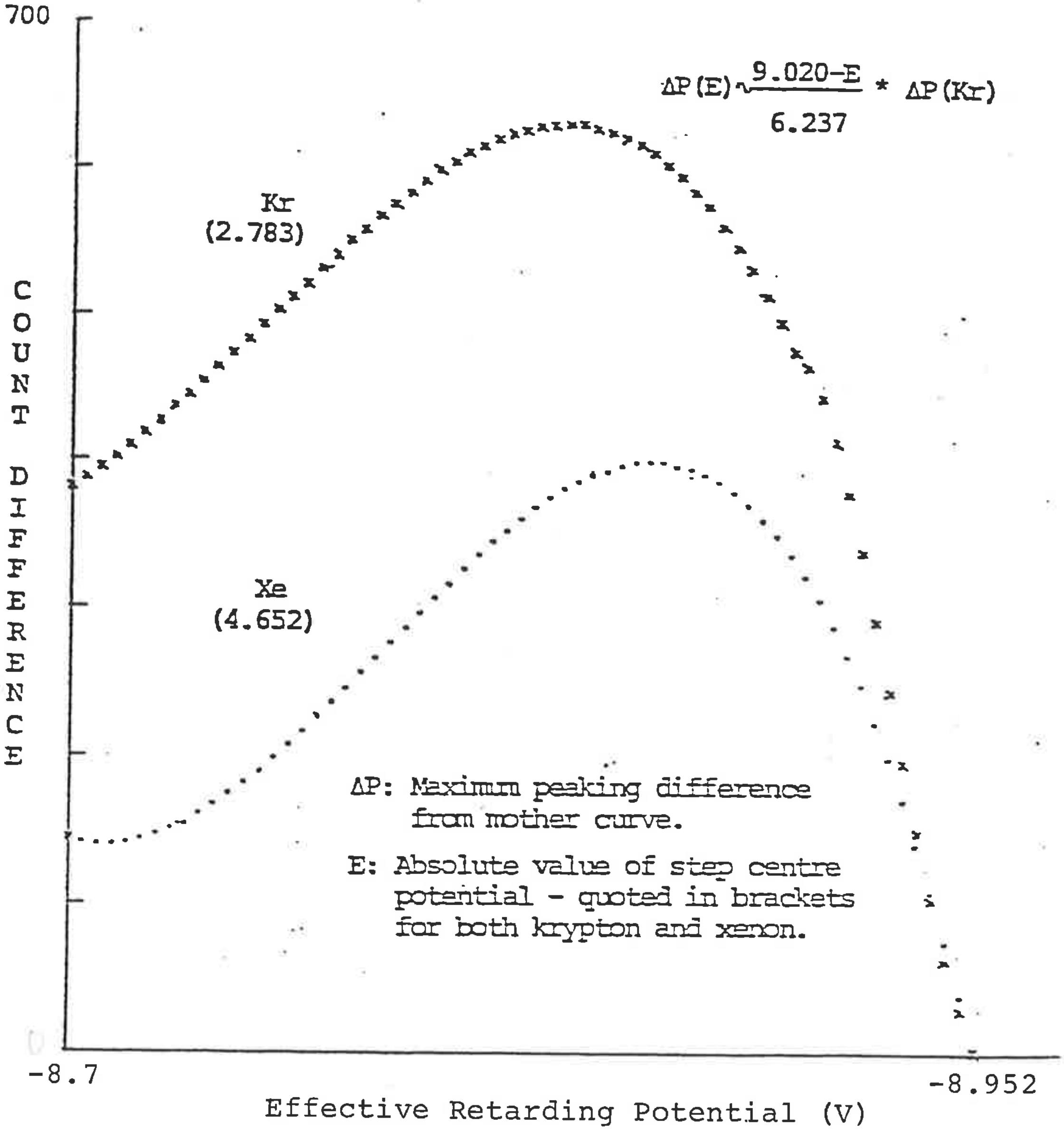

$\Delta P(E) \sim \frac{9.020 - E}{6.237} * \Delta P(Kr)$

ΔP: Maximum peaking difference from mother curve.

E: Absolute value of step centre potential - quoted in brackets for both krypton and xenon.

Figure IV.5 Smoothed peaking difference between the Xe mother curve and two lower energy curves after appropriate scaling of both axes. A value of 0 is forced at the peak turning point - strictly the slope should also be 0. The maximum difference scales quite well with the difference in absolute step centre potential from the mother curve (Table IV.3). The slight up-turn on the Xe curve is statistically insignificant - just a minor idiosyncrasy of the smoothing procedure.
NB. If the position of the maximum difference tends to vary significantly with step centre potential, on future plots, then the energy variation of the individual cubic parameters will have to be taken into account. Thus this part of the procedure would tend to a functional rather than numerical representation.

difference would be zero, but taking the difference as an error to be added, then a further linear energy relation for this would appear to be just about right. With a little care this technique could be extended to the lowest energies.

D) The Plateau

Once again, 'linear energy scaling' is employed, but this time curves are matched at zero potential, for position, and the minimum in the valley, for height. A significant error is expected, especially at low retarding potentials where the higher energy electrons are not always correctly focussed (Section III.2.2). But, again, a linear error-energy relation is adequate.

In the past, the two step argon plateau was thought to be representative of this region. But this cannot be true as the upper step is approached. Appendix III emphasises this point. Scans of the more extensive plateau regions between the xenon and krypton double steps provide the necessary fill-in.

IV.2.2a Proof that the Numerical Fit Works

Up to this point, I have described the basic methods of the numerical fit: dividing the step profile into four segments, scaling the energy axis appropriately and adding error curves where necessary. But this rather disjointed approach has yet to provide evidence that it really works. The following diagrams should supply the final verdict.

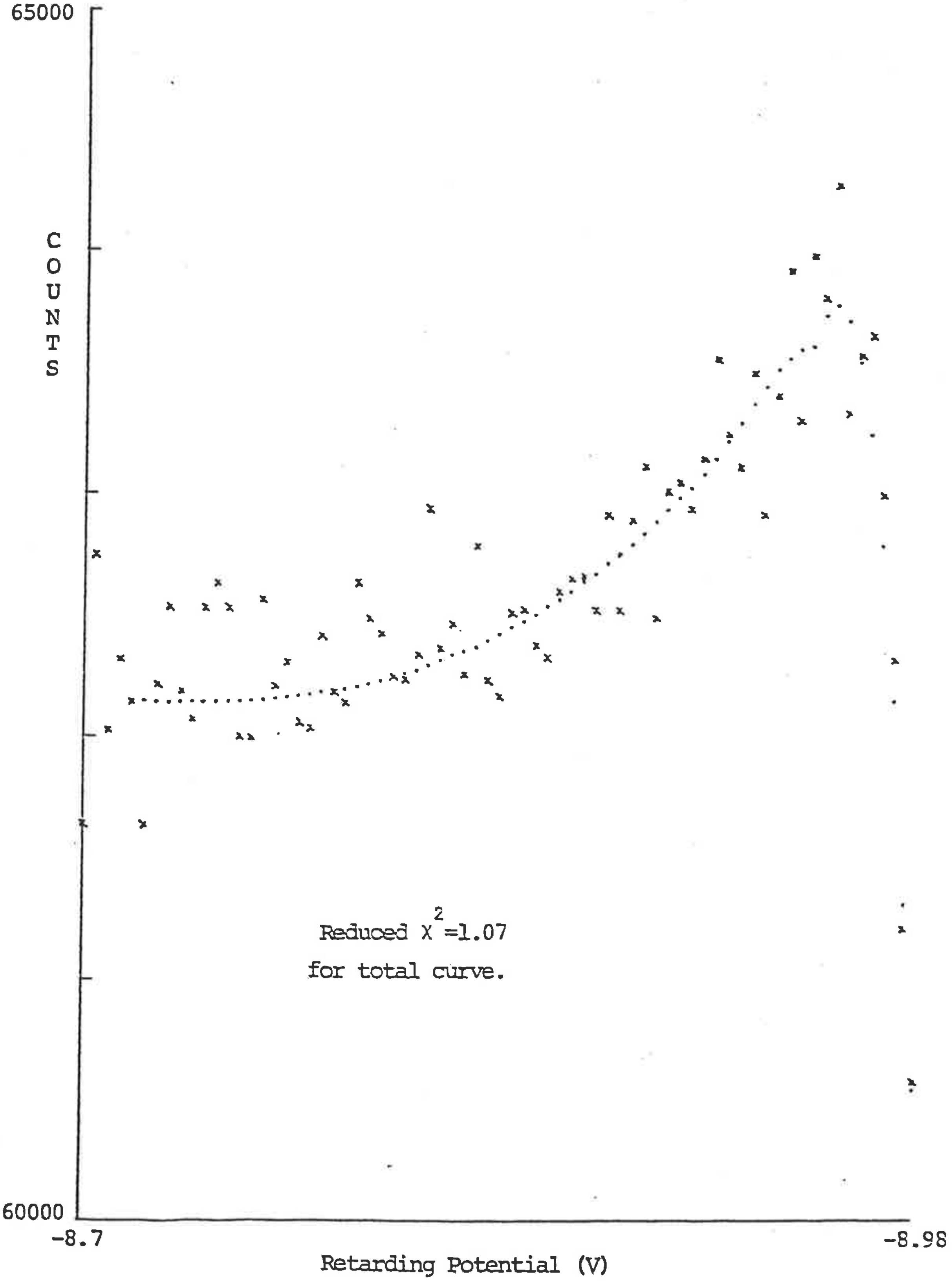

Figure IV.6 Detail from xenon at 58.4 nm fitted with smoothed background and unmodified mother curve.

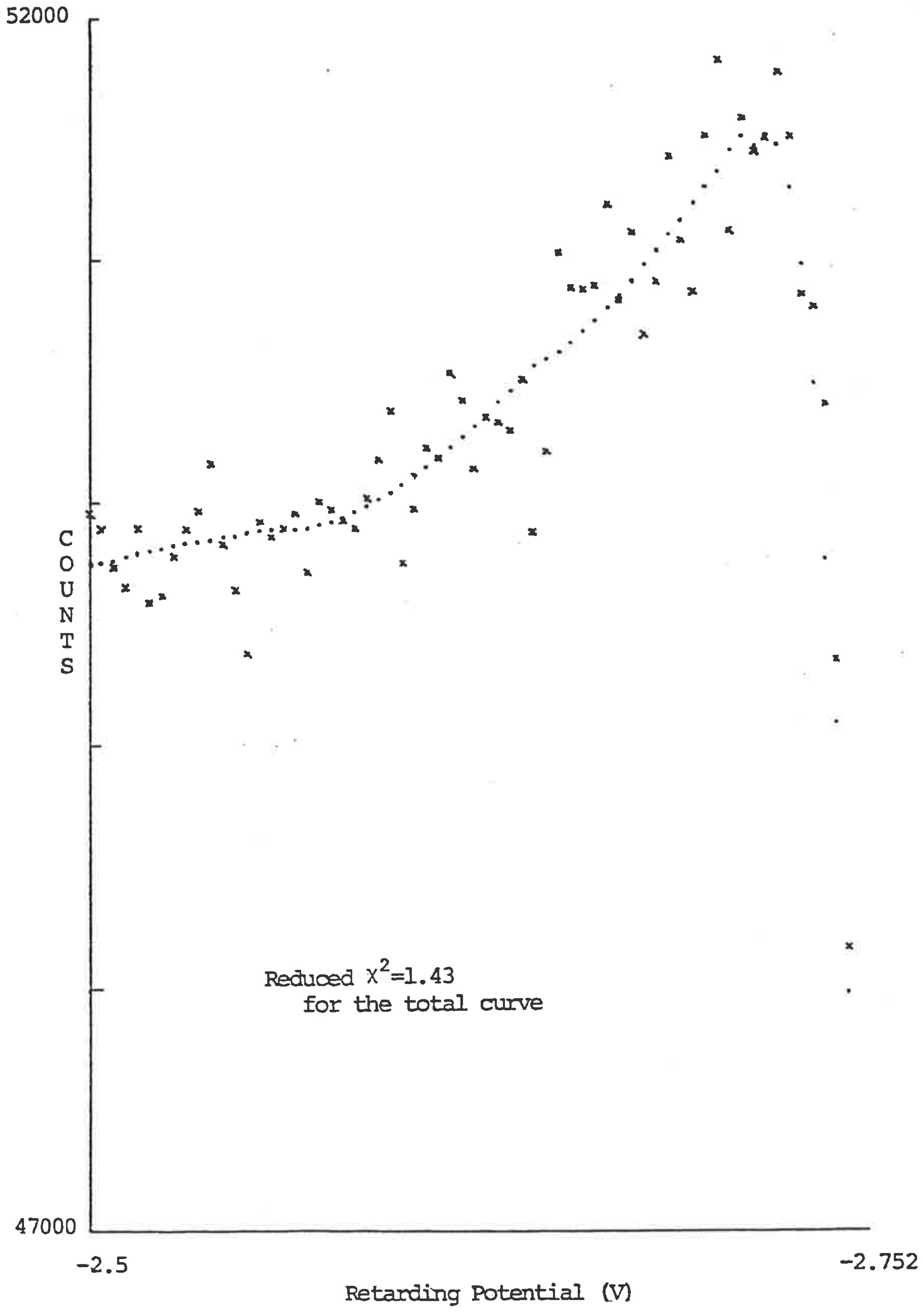

Figure IV.7 Detail from krypton at 73.6 nm fitted with smoothed background and modified mother curve. The chances of this being representative of a proper fit are less than 1 in 1000.

Figure IV.6 fits xenon 58.4 with it's smoothed background and unmodified mother curve. The excellent reduced χ^2 is not surprising. For any other curve, care must be taken to fit the right slope and shift (Figure IV.7). These cannot be found exactly enough from the two earlier graphs (Figures IV.2 & 4). Now the resultant red. χ^2 would appear to be rather poor. But the fit is still visually fine. In any event, we must not lose sight of our objectives, to fit multiple step data. There the individual steps are not nearly so well defined - about one-tenth the size at most and far less density of data points. So the fitting technique does not have to be nearly as accurate as a good fit of Figure IV.7 would have it. And besides, it is the simplicity of the method that really wins out, especially compared with the functional fit. The following two pages summarize the numerical fitting procedure.

SUMMARY OF NUMERICAL FIT PROCEDURE

A) Fitting a hypothetical single step with a true electron energy of 4eV (as found from differential photoelectron data). Scanned over 120 channels from -3.6 to -4.2V.

B) Provided with a smoothed mother curve of 250 channels from -8.7 to -9.2V. Peak turning point: 125.17 (-8.9503V). Step centre: 160.22 (-9.02044V). Also have a peaking error curve to be added to the first 126 channels of the mother curve.

C) Provided with a smoothed plateau curve of 51 channels from 0 to -5.1V, and an effective step centre (Appendix III) of -5.2149V. Plus an associated error curve.

1) Find the expected step centre from the shift function (Figure IV.4). Shift: 0.0653V gives a step centre of -3.9347V.

2) Error curves can be directly added to the unmodified mother and plateau; e.g., from Figure IV.5, $\Delta P=0.815*\Delta P(Kr)$.

3) Find relative slope compared with mother curve using slope function (Figure IV.2). Ratio: 15.653/14.041 gives expected T.P. at -3.8718V.

4) The modified peaking region range of the mother curve becomes -3.8718+(-3.9347)*(8.9503-8.7)/-9.02044 to -3.8718.i.e., -3.6815 to -3.8718V.

5) The modified plateau region range becomes 0 to -3.9347*-5.1/-5.2149. i.e., 0 to -3.8480. Importantly this overlaps with the peaking region.

6) The height of the plateau is rescaled to give a value of one in the valley minimum.

7) The height of the mother curve is rescaled to ensure a continuous curve at the initial point of overlap between plateau and peaking.

We are now ready to evaluate the expected normalised step shape beginning at a retarding potential of -3.6V, with K=0.

8) Test if peaking voltage range has been entered. If so then go to 9). Otherwise convert potential (V) to effective plateau channel number (N): N=V*51/-3.8480. **Now use interpolation to give relative height at this point. Store in S(K). V is now decremented by 0.02V and K incremented by 1. ** Repeat step 8).

9) Test if step edge region has been entered. If so then go to to 10). Otherwise convert potential to effective peaking channel: N=125.17*(V+3.6815)/(-3.8718+3.6815). **REPEATED** Repeat step 9).

10) Test if -4.2V has been reached. If so then go to 11). Otherwise convert potential to effective edge channel number: N=125.17+(V+3.8718)*(160.22-125.17)/(-3.9347 +3.8718). If N is greater than 250 then go to 11). **REPEATED** Repeat step 10).

11) The array elements S(K) for K from 0 to 120 now contain the expected step shape. Once the smoothed background has been subtracted from the data of interest (Section IV.2.2a), the same procedure can be used to scale S(K). The resultant scaling factor gives the height of the step. Reduced X^2 is a measure of the success of the entire effort.

IV.3 Step Height and the Efficiency Function

In Lindemans (1981, p.160), a quantitative measure of the analyser efficiency was made, using a continuum source. The method concentrated particularly on threshold electrons, using the lower step of the Inert gases. The calibration was arbitrarily made with respect to the point 100meV from the step centre. The efficiency was quoted as unchanging, from 300meV to 10eV, within "the uncertainty of the light monitors."

However, the results of this chapter, notably Section IV.2.2 on peaking, would appear to disprove constancy at the 100meV peaking point, though the error introduced is no doubt minor. Section III.2.2 suggests a point that moves with energy for calibration. As a continuum source is currently not available, no attempt has been made to prove this theory. But as no threshold electrons are looked at in this thesis, it seems safe to assume a constant efficiency and measure the height of any step at valley minimum.

CHAPTER V

V. EXPERIMENTAL RESULTS

We now have an easy technique for describing the analyser profile at any energy in the range from 1 to 9eV. It can be shown to be but a simple procedure to extend this to multiple steps, to accommodate the complex molecular spectra. There are complicating factors, however, through the appearance of rotational spreading and electronic spin-orbit splitting (in the case of oxygen), decidedly non-instrumental factors that must be allowed for. So how can these be overcome?

Given that they can, how do my results, in terms of branching ratios, compare with those in the literature? This is the true test of my procedure, not the reduced χ^2 values I might obtain.

V.I Fitting Multiple Step Data

Let us begin with a typical four-step oxygen spectrum (Figure V.1) recorded at 73.6nm, in equivalent fashion to the Inert gases previously. Now we have a way of portraying the single atomic step at any energy in the required range (3.9 to 5.0eV). In particular, the appropriate slopes and shifts can be adequately calculated from Figures IV.2 and IV.4, provided the true energy levels are known. Thus we should be able to obtain a set of four normalised curves and a smoothed background, which can be added together to mimic the analyser's multi-step response minus the constant photon background.

$$F(E_i) = a_0\, B^- (E_i) + a_1\, S_1(E_i) + a_2\, S_2(E_i) + a_3\, S_3(E_i) + a_4 S_4(E_i) \qquad \text{V.1}$$

B_s^- : smoothed background with photon level subtracted.
S_j : step shape with heights scaled to 1 in valley (Section IV.3).
a_j : height of step j - to be found.
E_i : energy of each channel from i=0 to 44.

If $B_s^-(E_i)$ is 'replaced' by $S_0(E_i)$, the above becomes highly suggestive of Equation IV.7, ensuring a solution by curve fitting as a very simple matter. The corresponding χ^2 is

$$\chi^2 = \sum_i \left(Y_i^- - \sum_{j=0}^{4} a_j\, S_{ji} \right)^2 / Y_i \qquad \text{V.2}$$

Y_i : original data

where (E_i) has been replaced by the i subscript. Partial differentiation w.r. to each of the a_j's leads to 5 homogeneous equations of the general form

$$2 \sum_i \left(Y_i^- - \sum_k a_k\, S_{ki}\right) S_{ji} / Y_i = 0 \qquad \text{V.3}$$

k : runs from 0 to 5.

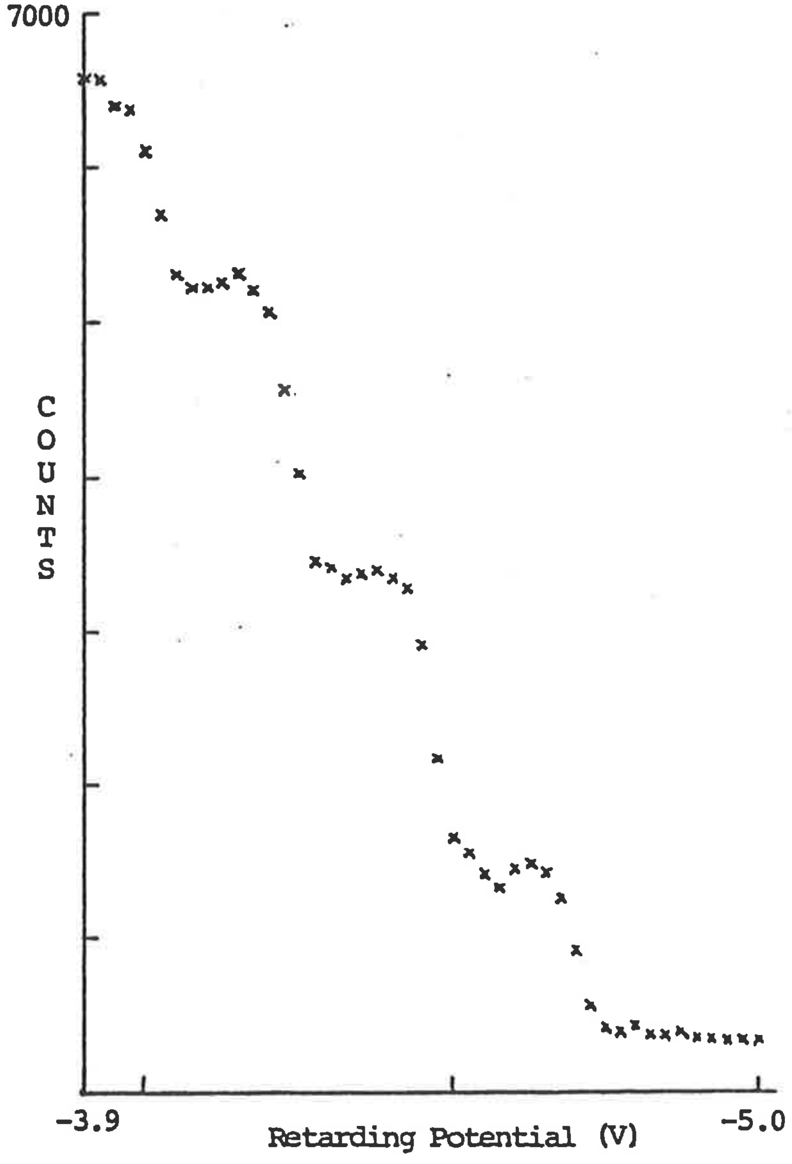

Figure V.1 Four lowest steps in oxygen at 73.6 nm.

These can be arranged more conveniently as

$$\sum_i Y_i^{-} S_{ji} / Y_i = \sum_k a_k \sum_i S_{ji} S_{ki} / Y_i \qquad \text{V.4}$$

which immediately suggests the elements in a matrix multiplication

$$\beta = a\alpha \qquad \text{V.5}$$

with

$$\beta_j = \sum_i Y_i^{-} S_{ji}/Y_i \qquad \text{V.6}$$

$$\alpha_{kj} = \sum_i S_{ji} S_{ki} / Y_i \qquad \text{V.7}$$

This can be solved for the only unknowns – the various step heights by the single matrix inversion mentioned in Section IV.2.

$$a = \beta \alpha^{-1} \qquad \text{V.8}$$

Noting that the error in any parameter can be found from the sum of the error contributions from each independent data point (Bevington, p.154), it can be shown that the inverted matrix contains the required error information.

$$\sigma^2(a_j) = \alpha_{jj}^{-1} \qquad \text{V.9}$$

More importantly, the uncertainties in the branching ratios must make allowance for the fact that the various heights are not found independently for integral data (Lindemans, 1981, p.305). Thus

$$\sigma^2\left(\frac{a_1}{a_2}\right) = \left(\frac{1}{a_2}\right)^2 \alpha_{11}^{-1} + \left(\frac{-a_1}{a_2{}^2}\right)^2 \alpha_{22}^{-1} + 2\left(\frac{1}{a_2}\right)\left(\frac{-a_1}{a_2^2}\right) \alpha_{22}^{-1} \qquad \text{V.10}$$

gives the uncertainty in the ratio a_1/a_2.

Of course, this entire section is perfectly applicable to spectra with other than four steps.

V.1.1 Problems with Molecular Spectra

The Inert gas spectra of the previous chapter were specifically chosen because they could best define the analyser response, nearly free of spreads relating to the type of gas used. This is no longer so for molecular spectra. Firstly, there is rotational spreading of the order of 5meV at room temperature. And, more critical in the case of oxygen, an electronic splitting of the ground state ion adds a further 23meV. The high resolution spectra of Samson and Gardner (1975) (Figure V.2a,b) clearly show both these effects.

Strictly the solution is a convolution of our standard atomic curves with the dual rotational envelopes. However, a simple approximation would appear to suffice. Firstly, Table V.1 provides all the relevant ionisation potential data.

TABLE V.1: THE FACTS FOR FITTING OXYGEN SPECTRA - THE GROUND STATE ION

Ionisation Potential	12.071	$^2\Pi_{\frac{1}{2}}$
for v_0	12.094	$^2\Pi_{\frac{3}{2}}$
Peak in Rotational band	2 meV higher	
Height Ratio $^2\Pi_{\frac{1}{2}}/^2\Pi_{\frac{3}{2}}$	0.93	

To obtain the ionising peak for the higher vibrational levels apply the following formula:

$$\text{Peak } (v_x) = 12.073 + x * 0.236 - 0.004 * x * (x+1)/2$$

This is accurate to at least level 15.

Now modelling each of the vibrational levels as two atomic levels, of slightly different height, placed the requisite 23meV apart, a remarkable fit is obtained (Figure V.3).

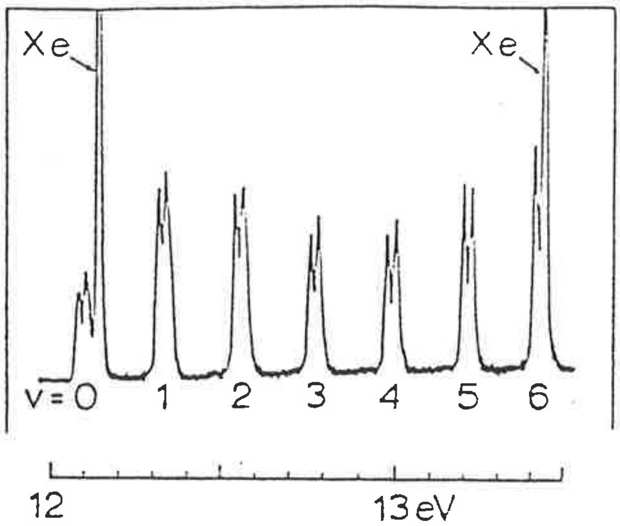

Figure V.2a Differential photoelectron spectrum of oxygen at 73.6 nm. The resolution 9 meV. Spin-orbit splitting is clearly evident. The xenon is used to calibrate the energy scale.

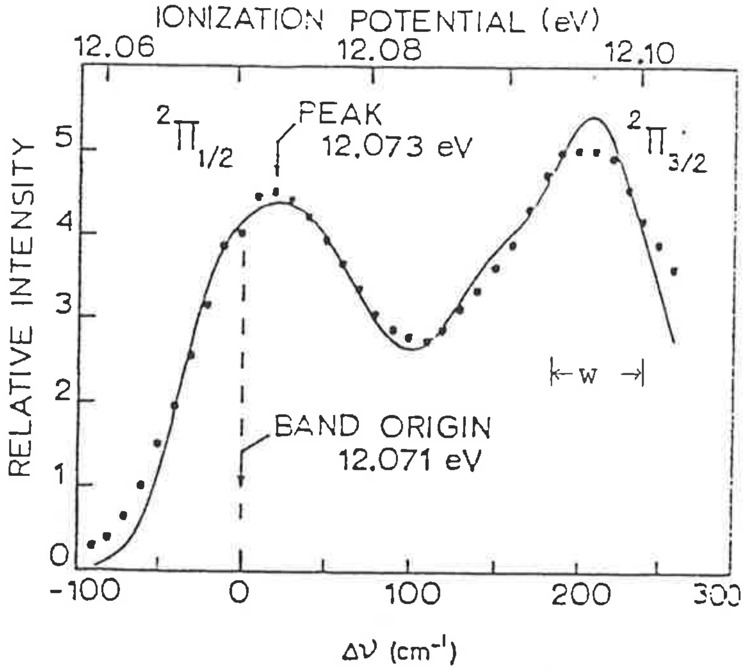

Figure V.2b Detailed photoelectron spectrum of the ground state of the oxygen ion (v=0). The solid curve is the calculated band shape taking into account the rotational structure. The resolution is 7 meV as indicated (w).

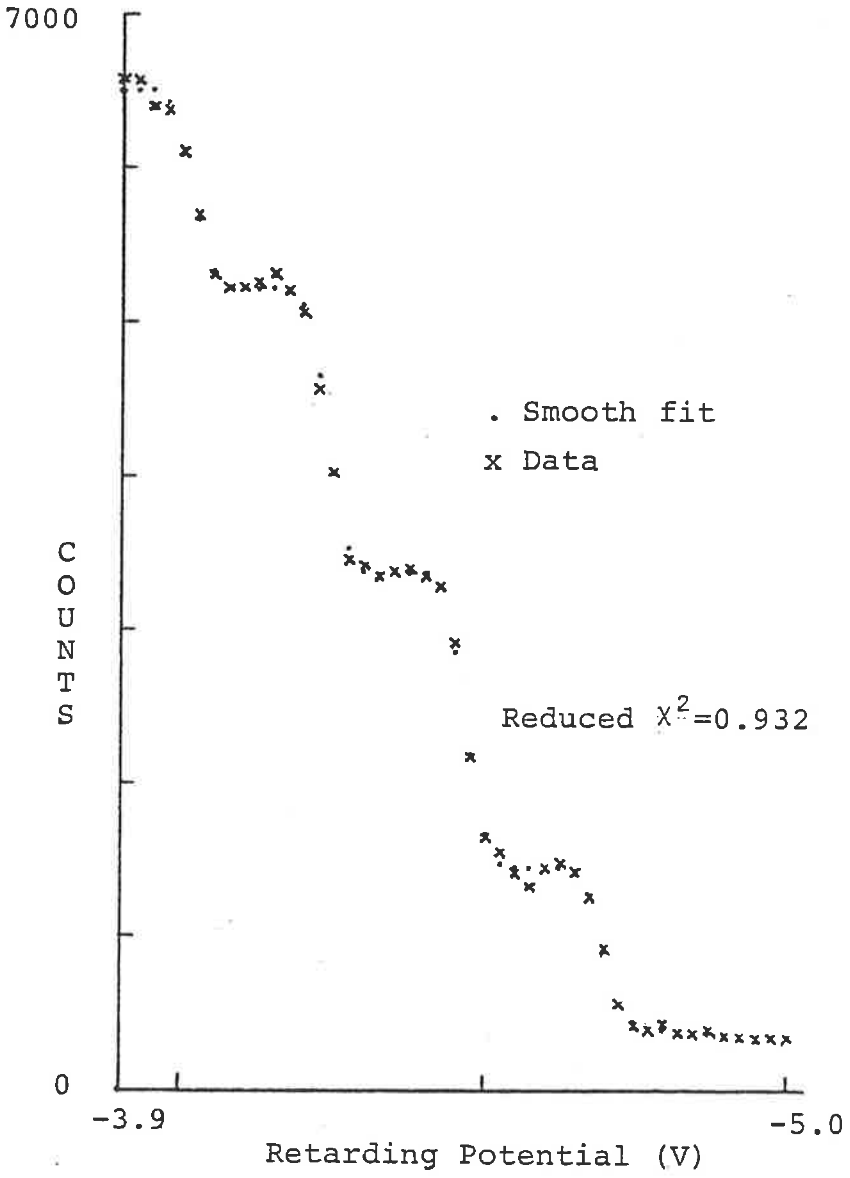

Figure V.3 Fit of four lowest steps in oxygen at 73.6 nm.

Table V.2a further analyses the viability of using two atomic levels by varying the splitting of the two. The best fit being at slightly less than 23meV is, no doubt, a statistical effect. Most importantly, the minor variation in the branching ratios with splitting, suggests there is little to be gained by the full convolution treatment.

No attempt has been made to exactly pin-point the correct energy shift, for each of the vibrational levels, as this would involve a complex non-linear fit. Table V.2b tests my simple approach by holding the splitting constant and 'manually' varying the shift. Little effect is evident over a 4meV range. A visual check should ensure you are using a shift within this range. Note also that the shift is a function of energy (Figure IV.4). But as such a weak function, any effects will be less than the above.

TABLE V.2a: THE EFFECTS OF SPLITTING ON PROFILE FITTING

Split meV	$100*(h_1/h_2)$	$100*\Delta(h_1/h_2)$	$100*(h_4/h_2)$	$100*\Delta(h_4/h_2)$	Reduced χ^2
0	52.98	1.41	67.81	2.58	1.016
10	53.03	1.41	67.82	2.59	0.986
20	53.03	1.42	67.93	2.60	0.932
23	53.02	1.42	67.99	2.60	0.934
30	52.98	1.43	68.16	2.62	1.031
40	52.89	1.45	68.46	2.65	1.527

TABLE V.2b: THE EFFECTS OF SHIFT ON PROFILE FIT

Shift meV	$100*({}^{h}1/h_2)$	$100*\Delta({}^{h}1/h_2)$	$100*({}^{h}4/h_2)$	$100*\Delta({}^{h}4/h_{\,2})$	Reduced χ^2
63.5	52.64	1.42	68.72	2.59	1.444
64.5	52.64	1.42	68.47	2.60	1.024
65.5	52.83	1.42	68.23	2.60	0.954
67.5	53.20	1.42	67.76	2.61	0.967
68.5	53.38	1.43	67.53	2.61	1.052
69.5	53.57	1.43	67.31	2.62	1.188

N.B. h_i is the height of step i.

V.2 Comparison with Literature

Figure V.5 graphically presents a comparison of the more reliable literature values with my own, of the branching ratios for the first 6 vibrational levels of oxygen at 58.4nm (Figure V.4). A few points should be taken into consideration here.

A) 'Reliable' usually means those that have allowed for the 'magic angle' (Section II.1) in collecting photoelectrons, something that many of the earlier experimentalists neglected. Problems may also arise through poor calibration.

B) Differential spectra dominate the literature, even for instruments which give integral statistics (Edqvist), 1970.

C) The possibility of pressure broadening of atomic line sources could lead to non-monochromacity, giving anomalous results in regions of significant partial cross-sectional variation due to autoionisation. The 58.4 line is safe in this respect, when using oxygen.

D) There is a disturbing, though understandable, reticence in quoting branching ratio errors throughout the literature. Instead comparison is generally made with some earlier effort. Gardner and Samson (1974) is the one exception presented here, though it is not quite clear how their errors are derived.

E) For my own part, the beauty of the curve fitting technique is that it provides the values and the statis-

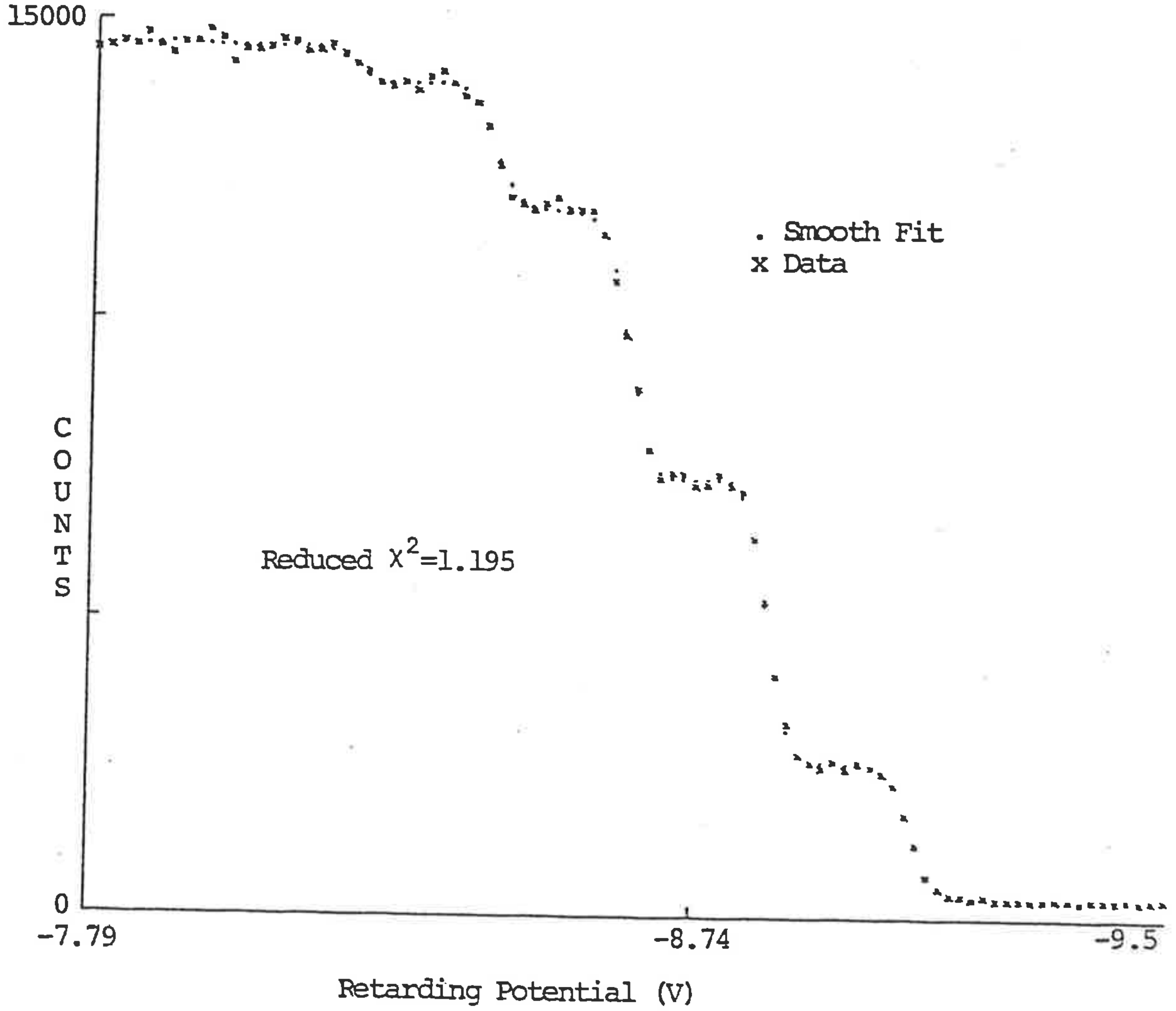

Figure V.4 Fit of six lowest levels in oxygen at 58.4 nm. The chances of this being a representative fit is 10%. (Section IV.2)

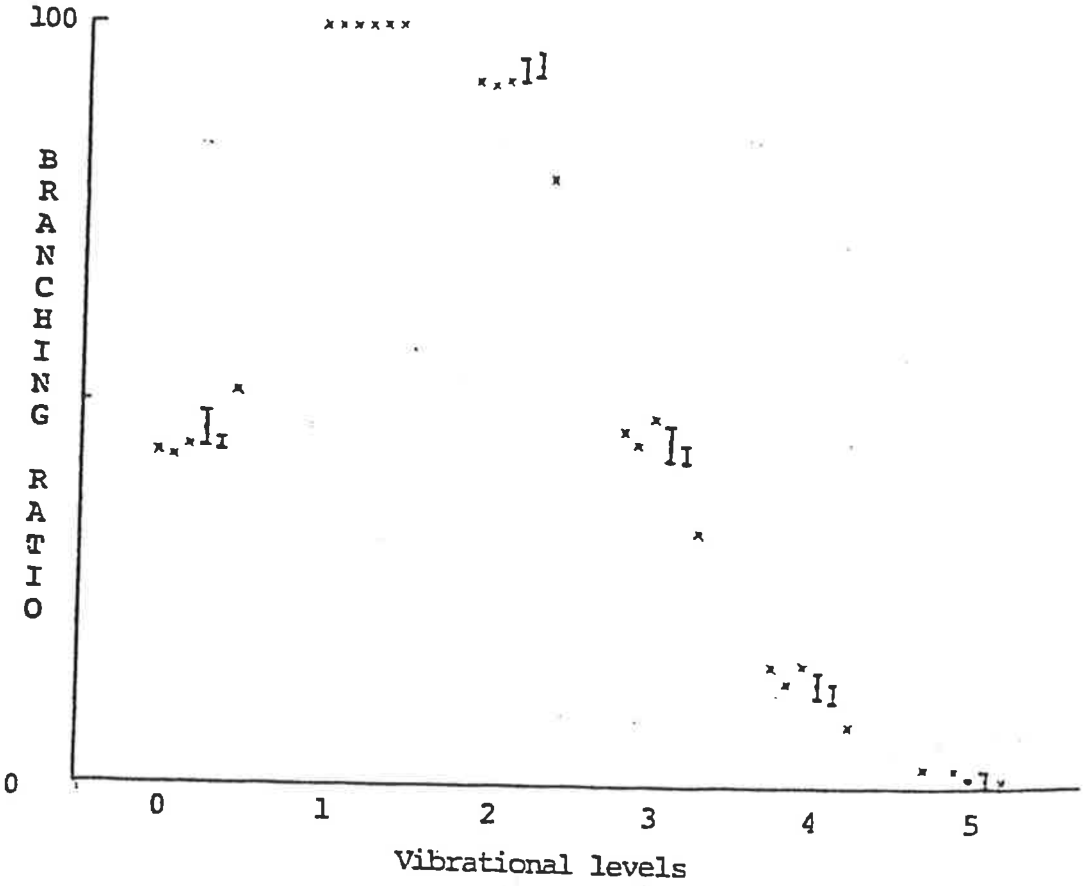

Figure V.5 Branching ratios for the first six levels in oxygen at 58.4 nm (as a % of v=1). Values from left to right for each level were obtained from -

Codling et al (1981) Average of 58.3-58.5 nm continuum scanning. (0.08 nm resolution) Hemispherical analyser.

Edqvist et al (1970) Spherical retarding in differential mode.

Kinsinger and Taylor (1973) Parallel plate spectrometer.

Gardner and Samson (1974) Cylindrical mirror analyser.

Present work.

Krupenie (1972) Franck-Condon factors.

tical errors all in one package. But, of course, these errors ignore any systematic blunders I may have made. Following Section IV.1 carefully should have guarded against most of these. But something that section does not cover is the efficiency variation of the system. This is where a comparison with other experimentalists becomes most useful.

So what can be said of Figure V.5? My approach appears to be well justified, certainly within the range of my statistical errors.

There is a side issue here that could be of some interest. Again returning to Figure V.5 it should be apparent that the Franck-Condon factors (Section I.2.1) are at clear variance with the experimental values. This has been taken as evidence of slight autoionisation at 58.4nm. Continuum wavelength scans of the total absorption cross-section, show a shallow trough, supporting this view (Lee _et_ _al_., 1973).

CHAPTER VI

VI. FUTURE PROSPECTS

Chapter V demonstrated a successful fit of oxygen at the 58.4nm atomic line. But the interest nowadays is in the whole range of wavelengths from 58.4 right up to 100nm, as found in the Hopfield helium continuum. This introduces the problem of non-monochromacity for continuum, as opposed to line, sources. The following relates the energy of a photon, in electron volts, to it's wavelength in nanometres.

$$E = h.c. / e. \lambda_n . 10^{-9} \qquad \text{VI.1}$$

c : velocity of light. $(m s^{-1})$
e : charge on electron. (C)
λ_n : wavelength in nm.

Thus for a given monochromator resolution, $\Delta \lambda_n$, the resulting energy spread is determined by

$$\Delta E = \Delta\lambda_n \quad A / \lambda^2_n \qquad \text{VI.2}$$

$$A = 1239.852 \quad (\lambda \text{ in nm}, \Delta E \text{ in eV})$$

With the monochromator exit and entrance slits set at 0.1mm, a resolution of 0.1nm has generally been used for continuum studies. This yields energy spreads of 34, 19 and 12meV for 60, 80 and 100nm, respectively. Now it would make sense to 'decrease' the resolution in the latter case, so that it approaches more nearly the typical electron analyser energy spread of 35meV. The intention would be to optimise the UV intensity, still a problem with continua, whilst ensuring the underlying instrumental response is not totally disrupted. Opening up the exit slit would achieve the desired result.

The same atomic response curves would still form the basis of continuum studies. And there seems no reason why the simple technique deployed for overcoming the 23meV splitting of oxygen, should not work equally well for continuum spreads. As for the proper interpretation of results, particular care must be taken in autoionising regions. This is a point well made by Gardner and Samson (1978), in comparing atomic and continuum branching ratio values. For such regions, continuous partial cross-sections are the order of the day (Lindemans, 1981, p.242).

In closing, three minor points should be made.

1) Hindsight would suggest that the fitting of a cubic to find the step edge's slope (Section IV.2.2b) as too exacting, especially when the edge can be seen as a not too critical part of the multi-step fitting routine. Much simpler, and far less time-consuming, is a width estimate with the step height found 'visually' (Figure III.3).

2) The simultaneous fit of several steps is not the only way to find branching ratios. Each step can be fitted quite well individually, the assumption being made that only the step under examination contributes significantly to the count variation in the 'neighbourhood' of the step. Thus the function to be fitted is

$$f(E_i) = a_0 + a_1 S_i \qquad \text{VI.3}$$

This is nigh on the simplest possible form for Equation V.1, allowing the unknowns, a_0 and a_1, to be found by the method of determinants (Bevington, p.106). A matrix inversion is unnecessary.

$$a_0 = \frac{1}{\Delta}\left(\Sigma \frac{S_i^2}{Y_i} \Sigma (1) - \Sigma \frac{S_i}{Y_i} \Sigma S_i\right) \qquad \text{VI.4a}$$

$$a_1 = \frac{1}{\Delta}\left(\Sigma \frac{1}{Y_i} \Sigma S_i - \Sigma \frac{S_i}{Y_i} \Sigma (1)\right) \qquad \text{VI.4b}$$

$$\Delta = \Sigma \frac{1}{Y_i} \Sigma \frac{S_i^2}{Y_i} - \left(\Sigma \frac{S_i}{Y_i}\right)^2 \qquad \text{VI.4c}$$

where the summations are over i, the relevant data points. The errors are given by

$$\sigma (a_0)^2 \simeq \frac{1}{\Delta} \Sigma \frac{S_i^2}{Y_i} \qquad \text{VI.5a}$$

$$\sigma (a_1)^2 \simeq \frac{1}{\Delta} \Sigma \frac{1}{Y_i}$$

This approach could be particularly useful for higher vibrational levels. In such a case, it would be unnecessary and wasteful to record all the levels.

3) An important extension of my work will be in looking at threshold electrons. The slope and shift functions of Figures IV.2 and 4. will no longer apply at the lowest energies, and the variation in efficiency (Figure III.5) can no longer be ignored.

APPENDICES

APPENDIX I MATHEMATICAL TECHNIQUES

There are a couple of mathematical techniques that find repeated use in the integral step analysis.

A) Smoothing

A cubic polynomial is curve fitted to a small segment of a data block - from channel I to channel K (a range of 10 to 100 channels). The polynomial form ensures a simple linear fit (Section IV.2).

$$F(x_i) = a_0 + a_1 x_i + a_2 x_i^2 + a_3 x_i^3 \qquad \text{AI.1}$$

where X_n now becomes x^n. i ranges through the integers from I to K. The value of x_i is unrelated to channel energy.

$$x_i = (i - I) / (K - I) \qquad \text{AI.2}$$

Clearly this ranges from 0 to 1, as you run through the points to be fitted. The reason for this is two-fold. The particular range tends to reduce computer round-off errors. And a starting value of 0 allows simple assignment of initial conditions.

$$F(0) = a_0 \qquad \text{AI.3a}$$

$$F'(0) = a_1 \qquad \text{AI.3b}$$

Upon fitting the cubic over a given range of channels, a corresponding reduced χ^2 is obtained. If this is much larger than 1 then the range generally must be reduced. The opposite applies for red. χ^2 less than one.

Once a satisfactory fit is obtained, the range is moved to an overlapping set of channels - J to L with $J \leq K$. Now to ensure a continuous fit, a_0 is simply set to $F(x_J)$ found from the previous range fit.

B) Interpolation

To find the most likely value at an energy between two channels, i and i+1, a cubic is directly fitted to the 4 channels from i to i+3. Note that the coefficients of the cubic are uniquely determined by the data values, Y(i) to Y(i+3), at these four channels. Care must be taken as the end of a data block is approached. The following bit of 'Basic programming' should make the above clear. Lower case characters are used for clarity.

```
10  REM Estimating the most likely data value at channel i+x
    where 0  <= x  <1 . 50 channels maximum.

15  i = INT (i+x) : IF i+x  =  50    THEN 45

20  IF   i+x > = 49    THEN 40

25  IF   i+x > = 48    THEN 35

30  I(3)  =  Y(i+3) - 3 * Y(i+2) + 3 * Y(i+1) - Y(i) : I(3) = I(3)/6

35  I(2)  =  Y(i+2)  - 2 * Y(i+1) + Y(i) - 6 * I(3) : I(2) = I(2)/2

40  I(1)  =  Y(i+1)  -  Y(1)  -  I(2)  -  I(3)

45  x  =  (i+x)  -  i  :  I(0)  =  Y(i)

50  IX  =  I(0)  +  I(1) * x  +  I(2) * x ↑ 2  +  I(3) * x ↑ 3
```

The interpolation works best on data that has already been smoothed.

APPENDIX II CBM PROGRAM GUIDE

The following provides a short description of each of the programs involved in the integral step analysis, in approximate order of their use.

PHOTOELECTRONS	Collects photoelectron data and stores individual cycles (Section IV.1).
PHOTON LEVEL	Similar to the above but specifically designed to find the constant photon background level.
PHOTO FINISH	Adds stored photoelectron cycles together. Individual cycles may be passed over if found wanting.
COMPARISON	For comparing curves at different pressures.
CURFIT	Non-linear curve fitting routine using Fermi-Dirac functions (Section IV.2.1).
SMOOTH BACK	Smooths and interpolates background data to match the number of main scan channels (Section IV.2.2).
SUBTRACT BACK	Subtracts smoothed background from main scan by appropriate scaling to tail section.
FIND SLOPE	Measures slope and height of single Inert gas steps.
SLOPE FUNCTION	Computes probable slope-energy relation (Figure IV.2).
MOTHER CURVE	Smooths single high resolution steps by curve fitting overlapping cubic segments. For mother curve or plateau.
SELF DRAWN	Smooths curves by visual fit of cubic.
INTERPOLATION	Rescales energy (channel) axis.
MINUS PLOT	Finds difference between two curves - used in peaking analysis (Section IV.2.2).
PEAK CURVE	Smooths peaking difference between two curves.
SINGLE STEP	Fits high resolution single steps by piecing together the four step segments, and thus testing the overall numerical fit routine (Section IV.2.2.a).

Xπ 02+	Finds the oxygem ground state ion's electron energy levels for a given wavelength.
BRANCHING RATIO	Fits multi-step data as of Chapter V.

The following provide a more general aid throughout analysis.

KYWD	High resolution graphics made easy.
DISPLAY	Visual display of 'any number' of data sets atop one another.
PRINTER	Hard copy printout of the above.
REFILE	Allows data sets to be modified to more convenient forms.
POISSEL	Tests statistics of channeltron.

APPENDIX III THE PLATEAU

The plateau for a single step ranges from 0 retarding potential to the valley minimum (Figure III.3). To obtain a representative curve in this region the plateau atop the two steps of argon has been used in the past. The appropriate step centre must arise from a weighted average of the two step centres involved (Figure AIII.1a). Ideally the plateau should be representative of that arising from a single step at the weighted step centre. This is effectively true for the lower retarding potentials but as the upper step is approached it must dominate the response. A better description of the plateau region near a step is provided by the space between the well separated spin-orbit components of krypton (0.666eV split) and xenon (1.306) (Figure AIII.1b). For high energy steps (step centres ∿ 9eV) argon with the He 30.4nm line may be needed to define the plateau.

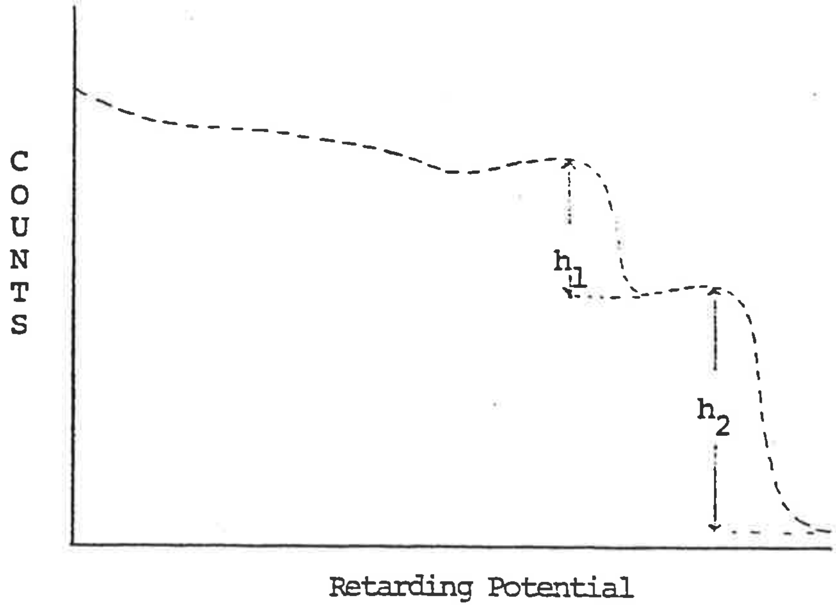

Figure AIII.1a The appropriate step centre for the plateau in argon at 58.4 nm is given by-

$$S.C. = \frac{5.281*h_1}{h_1+h_2} + \frac{5.458*h_2}{h_1+h_2} \text{ eV}$$

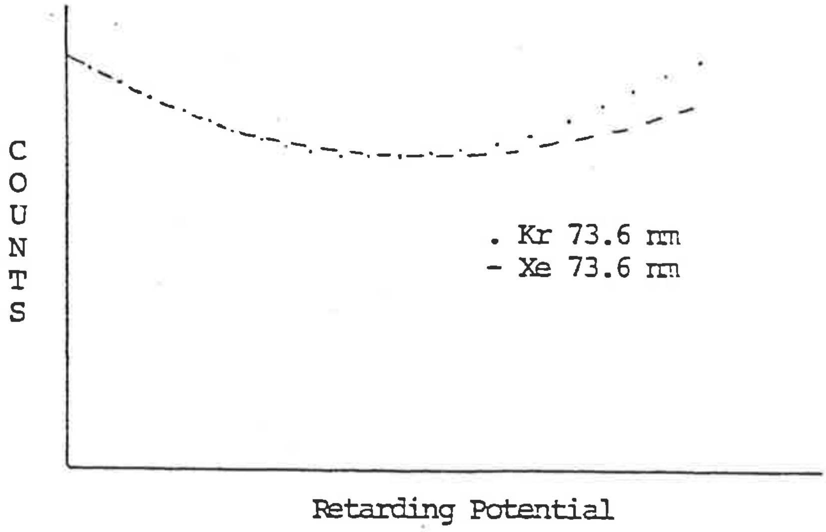

Figure AIII.1b Exaggeration of the valley regions after the two curves have been energy normalised and matched for valley height. Note that in the fitting routine there is no sharp distinction between plateau and peaking - the two regions simply merge together. The difference in the two curves results in an error curve. For the lower retarding potentials the argon plateau is used after energy normalisation and valley height match-up to the above curves.

REFERENCES

REFERENCES

Banwell, C.N. (1972) Fundamentals of Molecular Spectroscopy, Chap. 5, (McGraw-Hill).

Bevington, P.R. (1969) Data Reduction and Error Analysis for the Physical Sciences, (McGraw-Hill, N.Y.).

Born, M. and Oppenheimer, R. (1927) Ann. Physik., Vol. 84, p.457.

Codling, K., Parr, A.C., Stockbauer, R.L., West, J.B., Dehmer, J.L. (1981) J. Phys. B: Atom. & Molec. Phys., Vol. 14, p.657.

Dehmer, P.M. and Chupka, W.A. (1975) J. Chem. Phys., Vol. 62, p.4525.

Edqvist, O., Lindholm, E., Stein, L.E., Asbrink, L. (1970) Physica Scripta, Vol. 1, p.1970.

Fano, U. (1961) Phys. Rev., Vol. 124, p.1866.

Fock, V. (1930) Z. Physik. Vol. 61, p.126.

Frost, L.S. and Phelps, A.V. (1964) Phys. Rev., Vol. 136, p.A1538.

Gardner, J.L. and Samson, J.A.R. (1974) J. Chem. Phys., Vol. 61, p.5472.

Gardner, J.L. and Samson, J.A.R. (1973) J. Elec. Spec. & Rel. Phenom., Vol. 2, p.267.

Gardner, J.L. and Samson, J.A.R. (1978) J. Elec. Spec. & Rel. Phenom., Vol. 13, p.7.

Hartree, D.R. (1928) Proc. Cambridage Phil. Soc., Vol. 24, p.111.

Herzberg, G. (1950) Molecular Spectra and Molecular Structure I. Spectra of Diatomic Molecules, (Van Nostrand Reinhold Company).

Huffman, R.E., Larrabee, J.C., Chambers, D. (1965) Appl. Optics, Vol. 4, p.1145.

Huffman, R.E., Tanaka, Y., Larrabee, J.C. (1963) J. Chem. Phys. Vol. 39, p.902.

Hutton, J.M. (1981) An Apparatus for Partial P.I. Cross-Section Measurements, Masters, Adel. Uni.

Jones, A.L. (1982) Photodissociation Spectroscopy, Hons. Report, Adel. Uni.

Kinsinger, J.A. and Taylor, J.W. (1973) Int. J. Mass Spec. & Ion Phys., Vol. 11, p.461.

Krupenie, P.H. (1972) J. Phys. Chem. Ref. Data, Vol. 1, p.423.

Lee, L.C., Carlson, D.W., Judge, D.L., Ogawa, M. (1973) J. Quant. Spec. & Rad. Trans., Vol. 13, p.1023.

Lindemans, W. (1981) Photoionisation of Diatomic Molecules, Ph.D. Thesis, Adel. Uni.

Lu, K.T. (1971) Phys. Rev. A, Vol. 4, p.579.

Manson, S.T. (1978) Topics in Applied Physics, Vol. 26; Ed: Cardona, M., Ley, L. (Springer-Verlag).

Marr, G.V. (1967) Photoionisation Processes in Gases, (Academic Press).

Marr, G.V. (1968) Plasma Spectroscopy, (Elsevier).

Martin, B. (1981) Honours Report, Adel. Uni.

Merchant, V.E., Seguin, H.J.J., Dow, J. (1978) Rev. Sci. Instrum. Vol. 49, p.1631.

Mies, F.H. (1968) Phys. Rev., Vol. 175, p.164.

Morse, P.M. (1929) Phys. Rev., Vol. 34, p.57.

Parker, Jr. J.H. and Warren, R.W. (1962) Rev. Sci. Instrum., Vol. 33, p.948.

Samson, J.A.R. (1978) Nucl. Instrum. & Methods, Vol. 152, p.225.

Samson, J.A.R. and Gardner, J.L. (1975) Can. J. Phys., Vol. 53, p.1948.

Samson, J.A.R. and Gardner, J.L. (1977) J. Chem. Phys., Vol. 67, p.755.

Schiff, L.I. (1981) Quantum Mechanics, (McGraw-Hill).

Smith, A.L. (1970) Phil. Trans. Roy. Soc. (London), Vol. A268, p.169.

Stelle, D., Lippincott, E., Vanderslice, J. (1962) Rev. Mod. Phys., Vol. 34, p.239.

Tanaka, Y. (1942) Sci. Papers, Inst. Phys. Chem. Res. (Tokyo), Vol. 39, p.465.

Thyratron Preamble (1972) English Electric Valve Company Ltd.

Torop, L. (1975) Daresbury Laboratory Report, DL/SRF/R5.

Turner, D.W. (1968) Proc. Roy. Soc. (London), Vol. A307, p.15.

West, J.B., Codling, K., Marr, G.V. (1974) J. Phys. E: Sci. Instrum., Vol. 7, p.137.

Yang, C.N. (1948) Phys. Rev., Vol. 74, p.764.